Monthly Notices of the ROYAL ASTRONOMICAL SOCIETY

MNRAS **478,** 548–567 (2018) doi:10.1093/mnras/sty774
Advance Access publication 2018 March 23

Quenching and ram pressure stripping of simulated Milky Way satellite galaxies

Christine M. Simpson,[1⋆] Robert J. J. Grand,[1,2] Facundo A. Gómez,[3,4,5] Federico Marinacci,[6] Rüdiger Pakmor,[1] Volker Springel,[1,2] David J. R. Campbell[7] and Carlos S. Frenk[7]

[1] *Heidelberger Institut für Theoretische Studien, Schloss-Wolfsbrunnenweg 35, D-69118 Heidelberg, Germany*
[2] *Zentrum für Astronomie der Universität Heidelberg, Astronomisches Recheninstitut, Mönchhofstr 12-14, D-69120 Heidelberg, Germany*
[3] *Max-Planck-Institut für Astrophysik, Karl-Schwarzschild-Str 1, D-85748, Garching, Germany*
[4] *Instituto de Investigación Multidisciplinario en Ciencias y Tecnología, Universidad de La Serena, Raúl Bitrán 1305, La Serena, Chile*
[5] *Departamento de Física y Astronomía, Universidad de La Serena, Av. Juan Cisternas 1200 Norte, La Serena, Chile*
[6] *Department of Physics, Kavli Institute for Astrophysics and Space Research, MIT, Cambridge, MA 02139, USA*
[7] *Institute for Computational Cosmology, Department of Physics, Durham University, South Road, Durham DH1 3LE, UK*

Accepted 2018 March 19. Received 2018 March 19; in original form 2017 May 7

ABSTRACT

We present predictions for the quenching of star formation in satellite galaxies of the Local Group from a suite of 30 cosmological zoom simulations of Milky Way-like host galaxies. The Auriga simulations resolve satellites down to the luminosity of the classical dwarf spheroidal galaxies of the Milky Way. We find strong mass-dependent and distance-dependent quenching signals, where dwarf systems beyond 600 kpc are only strongly quenched below a stellar mass of 10^7 $M_\odot$. Ram pressure stripping appears to be the dominant quenching mechanism and 50 per cent of quenched systems cease star formation within 1 Gyr of first infall. We demonstrate that systems within a host galaxy's R_{200} radius are comprised of two populations: (i) a first infall population that has entered the host halo within the past few Gyrs and (ii) a population of returning 'backsplash' systems that have had a much more extended interaction with the host. Backsplash galaxies that do not return to the host galaxy by redshift zero exhibit quenching properties similar to galaxies within R_{200} and are distinct from other external systems. The simulated quenching trend with stellar mass has some tension with observations, but our simulations are able reproduce the range of quenching times measured from resolved stellar populations of Local Group dwarf galaxies.

Key words: galaxies: dwarf – galaxies: groups: general – galaxies: interactions – Local Group – galaxies: star formation – cosmology: theory.

1 INTRODUCTION

The Milky Way (MW) galaxy and M31 host systems of satellite dwarf galaxies that have been of great interest in recent decades because of the perceived challenges they pose to Λ cold dark matter (ΛCDM) in terms of their number (Klypin et al. 1999; Moore et al. 1999), structure (Boylan-Kolchin, Bullock & Kaplinghat 2011) and spatial distribution (Ibata et al. 2013). These systems also pose challenges to models of galaxy formation, as many appear to be some of the most dark matter dominated objects in the Universe (McGaugh et al. 2010). Studies of resolved stellar populations in these systems have shown a diversity of star formation histories and provided a local window into the high-redshift Universe by constraining these histories over 12 Gyr (e.g. Weisz et al. 2014). A holistic cosmological model of the Local Group needs to explain not only the many structural properties of satellite galaxies but also their star-forming properties over a Hubble time.

Properties of dwarf galaxies in the Local Group exhibit strong trends with both luminosity and environment. There is a clear metallicity–luminosity trend that may indicate strong galactic winds in these systems (Kirby, Martin & Finlator 2011). There is a strong correlation between distance from either the MW or M31 and gas content. Few satellites within 270 kpc of either the MW or M31 contain detectable H I gas and most systems beyond this distance do contain H I (Grcevich & Putman 2009), sometimes in significant amounts (Ryan-Weber et al. 2008). There is also a strong correlation between distance and galaxy type in the Local Group (Grebel 1999) that may connect to distance trends for intermediate luminosity dwarfs (with stellar masses above 10^7 $M_\odot$), where most systems

⋆ E-mail: christine.simpson@h-its.org

in the field are found to be star forming and of late type (Geha et al. 2012). A small population of early-type field dwarfs are known, although at lower luminosities (Makarova et al. 2017).

Within the Local Group, the satellite populations of the MW and M31 exhibit some striking differences. For example, M31 contains several dwarf elliptical (dE) galaxies, while the MW has none (McConnachie 2012). Also, M31 contains several dwarf spheroidal (dSph) galaxies with unusually large half-light radii compared to MW dSphs (Collins et al. 2013). The MW contains the Magellanic clouds, two nearby, gas rich and actively star-forming dwarf irregular (dIrr) galaxies, that are the main exceptions to the distance trends otherwise observed in the Local Group. There are also differences in the globular cluster populations around the MW and M31 (Huxor et al. 2011). A possible explanation for these differences is cosmic variance, i.e. the statistical variance in the dark matter assembly histories of two otherwise similar dark matter haloes. A theoretical exploration (e.g. in simulations) of satellite properties in the context of the Local Group therefore needs to account for cosmic host variance.

To date, most simulation studies of MW analogue satellite systems have typically focused either on one to a few high-resolution cosmological models with gas physics (Okamoto et al. 2010; Zolotov et al. 2012; Wetzel et al. 2016) or have focused on a large suite of dark matter only models that better probe cosmic variance, but do not include the effects of baryons (Garrison-Kimmel et al. 2014; Hellwing et al. 2016). An exception is the APOSTLE simulations, a set of 12 cosmological zoom simulations of Local Group-like volumes (Fattahi et al. 2016; Sawala et al. 2016a,b). These simulations have demonstrated the impact of reionization and tidal stripping on dwarf satellites with a model that includes both gas physics and dark matter across a large sample of dwarf satellite systems.

The physics that shapes the star formation histories of satellite galaxies is diverse, but interaction with the host galaxy likely plays an important role through both tidal effects and ram pressure stripping (Gatto et al. 2013; Emerick et al. 2016; Zhu et al. 2016). The shallower gravitational potentials of these systems boost the impact of feedback processes and, at very low masses, reionization likely plays an important role (Efstathiou 1992; Thoul & Weinberg 1996; Benson et al. 2002).

The goal of this study is to identify the physical mechanisms that drive quenching in Local Group satellite galaxies at the luminosity scale of the 'classical' dSphs, which are well-studied observationally. To do this, we will use the simulations of the Auriga project, a suite of 30 cosmological, hydrodynamical simulations of MW-like galaxies (Grand et al. 2017). Our aim will be to quantify patterns in quenching and gas loss among subhaloes within a local volume around the simulated host galaxies (<1 Mpc) and explore the processes, such as ram pressure stripping, that shape these patterns. We will then quantify time-scales for gas loss and quenching and compare these time-scales to the infall histories of systems in order to better understand how the final quenching patterns emerge over time. The perspective of this study is that of the surviving, luminous satellite dwarf galaxy. Systems that are tidally destroyed before $z = 0$ and systems that are dark or have underresolved stellar populations are also interesting, but will be addressed in later work.

The structure of this paper is as follows. In Section 2, we describe the Auriga simulations and their galaxy formation model. In Section 3, we examine the properties of surviving luminous subhaloes across the simulation sample, and in Section 4, we turn to the physical processes responsible for these properties, with a particular focus on ram pressure stripping. Section 5 contains an exploration of time-scales associated with quenching and the connection between quenching and subhaloes' orbital histories. In Section 6, we discuss how our results compare to observations and we present conclusions in Section 7.

2 METHODS

The 30 'Level 4' simulations of the Auriga project (Grand et al. 2017) are the simulation sample we use to investigate dwarf galaxy quenching in the Local Group. Here, we describe the Auriga simulations' set-up and physical model and the analysis techniques, such as merger tree finding, that we use for later analysis.

2.1 The Auriga simulations

The Auriga project consists of cosmological zoom-in simulations of $\sim 10^{12}$ $M_\odot$ dark matter haloes within the ΛCDM paradigm conducted with the second-order accurate moving mesh code AREPO (Springel 2010; Pakmor et al. 2016). All simulations include collisionless dark matter; ideal magnetohydrodynamics with a Powell cleaning scheme (Powell et al. 1999; Pakmor, Bauer & Springel 2011); primordial and metal-line cooling (Vogelsberger et al. 2013); a subgrid model for the interstellar medium (ISM) that employs a stiff equation of state representing a two-phase medium in pressure equilibrium (Springel & Hernquist 2003); a model for star formation and stellar feedback, including a phenomenological wind model and metal enrichment from SNII, SNIa and AGB stars (Vogelsberger et al. 2013); the formation of black holes and feedback from active galactic nuclei (Springel, Di Matteo & Hernquist 2005a; Marinacci, Pakmor & Springel 2014; Grand et al. 2017); and a spatially uniform but time-varying UV background that completes reionization at redshift 6 (Faucher-Giguère et al. 2009; Vogelsberger et al. 2013).

Each Auriga host halo was selected from a cosmological dark-matter-only simulation of the EAGLE project (Schaye et al. 2015). The parent cube has a side length of 100 comoving Mpc and cosmological parameters $\Omega_m = 0.307$, $\Omega_b = 0.048$, $\Omega_\Lambda = 0.693$, and $h = 0.6777$ (Planck Collaboration XVI 2014). Candidate haloes were required to fall within a narrow range of final virial halo mass around 10^{12} $M_\odot$.

A weak isolation criterion was used to select candidate haloes that required the closest halo of equivalent or larger mass to be at least $9R_{200}$ lengths distant (R_{200} is defined as the radius within which the halo's mean density is equal to 200 times the critical density of the universe). This isolation criterion did not impose any restrictions on selected haloes' substructure. In some cases, the selected haloes host massive subhaloes that contain large galaxies themselves (e.g. Au1 has a nearly equal mass companion within R_{200}). The process for host halo selection is described in more detail by Grand et al. (2017).

Zoom initial conditions were created for each selected Auriga host halo following the procedure of Jenkins (2010). The region of interest, containing the host halo and a surrounding buffer region with many other smaller haloes, is simulated with lower-mass dark matter particles, while the rest of the box is simulated with higher-mass dark matter particles. In most of the 30 zoom simulations, the closest low-resolution particle to the host halo is more than $4R_{200}$ distant and, in all cases, more than $3R_{200}$ distant.

High-resolution dark matter particles have a mass of $\sim 3 \times 10^5$ $M_\odot$. Gas cells have a target mass of $\sim 5 \times 10^4$ $M_\odot$, and therefore, both gas cells and star particles have masses within a factor of 2 of this value. Gravitational forces for star particles

and high-resolution dark matter particles are computed with a comoving softening length of $500\,h^{-1}$pc until $z = 1$, after which a constant physical softening length of 396 pc is used. Gravitational forces for gas cells are computed with a softening length that scales with the mean cell radius, but limited to be between the star particle softening length and 1.85 physical kpc.

2.2 Simulation data and analysis

All 30 Auriga simulations are denoted by the descriptor 'AuN', where N varies between 1 and 30. Each simulation produces 128 full snapshots with contemporaneous halo catalogues that have a maximum spacing between snapshots of 167 Myr that decreases towards higher redshift. All simulations were run with the in-simulation halo finder SUBFIND (Springel et al. 2001) that identifies central haloes with a friends-of-friends (FOF) algorithm (Davis et al. 1985) and gravitationally bound subhaloes.

The spherical region uncontaminated by low-resolution dark matter particles extends out to $4R_{200}$ in most of the simulations; however, due to the web-like structure of dark matter on the scale of Mpcs, the high-resolution Lagrangian region is irregular and almost all of the haloes and subhaloes with 1 Mpc of the main halo are uncontaminated. We judge whether a subhalo is contaminated by measuring the number of low-resolution dark matter particles within $3r_{200}^{\rm subhalo}$, where $r_{200}^{\rm subhalo}$ is defined for each subhalo as the radius within which the average subhalo density is 200 times the critical density of the universe in the same way R_{200} is defined for the host halo. Any subhalo that has coarse resolution dark matter particles within $3r_{200}^{\rm subhalo}$ is considered to be contaminated. In all 30 simulations, only one subhalo within 1 Mpc at $z = 0$ in one simulation (Au15) was found to be contaminated. We exclude it from our analysis.

In post-processing, merger trees were constructed with the LHaloTree algorithm that creates a merger linking between successive halo catalogues, including subhaloes of central haloes (Springel et al. 2005b). The version of LHaloTree applied here includes a modification of the traditional algorithm that uses a cumulative sum of all of a subhalo's ancestors' masses (computed recursively) to distinguish the primary progenitor among all progenitors of a given generation. This improvement reduces discontinuous jumps in properties along a halo's main ancestral line (De Lucia & Blaizot 2007).

For the purpose of visualizing some of the fast moving processes that operate on time-scales less than 200 Myr, such as ram pressure stripping of satellites, we re-ran Au6 with the same mass resolution, but with an increased number of snapshots (1024 outputs rather than 128). This resimulation has a maximum time between successive snapshots of 21 Myr. The satellite distribution in this simulation has some small differences in the orbital histories of the satellites due to the differences in the time-step hierarchy necessitated by the higher frequency of outputs, but the overall satellite distribution is statistically similar to that of the original simulation. The visualizations presented in Fig. 8 were created with this simulation.

3 PROPERTIES OF SURVIVING SUBHALOES

In all 30 of the Auriga zoom simulations, the host halo contains both luminous and dark subhaloes at redshift zero; here, we describe the overall number and general baryon properties of these structures. Fig. 1 shows the environment around an example host (in Au6) and the distribution of subhaloes found within 1 Mpc. First, it is evident that the host halo lies at the intersection of several dark matter filaments and that suhaloes preferentially lie along these filaments. Secondly, it is clear from the projections of star particles and gas that most of these subhaloes are dark and gas poor. Thirdly, the complex structures in stars at distances of tens to hundreds of kpc from the host's disc indicate that many subhaloes have been tidally destroyed and the population of subhaloes examined here are just the survivors of a continuous process of subhalo accretion and destruction. We will discuss the physical mechanisms that result in these properties and associated time-scales in Sections 4 and 5.

Table 1 lists general properties the subhalo systems at redshift zero, such as the number of luminous subhaloes within 300 kpc and 1 Mpc, the fraction of 'quenched', non-star forming subhaloes, and the fraction of gas-poor subhaloes. These properties, and all subsequent analysis, are restricted to subhaloes that have a minimum total mass of $10^8\,{\rm M}_\odot$, a minimum stellar mass of $5 \times 10^5\,{\rm M}_\odot$ within twice the half stellar mass radius ($r_{1/2}$), and a minimum dark matter mass of $10^6\,{\rm M}_\odot$. This last requirement is intended to exclude from our analysis star-forming gas clumps spuriously detected by the SUBFIND algorithm, which aims to identify dark matter structures. When referring to a subhalo's stellar mass, we mean the stellar mass within $2r_{1/2}$ and when referring to a subhalo's total mass, we mean the mass of all resolution elements linked to the subhalo by SUBFIND.

The stellar mass cut that we have applied is ten times the target gas mass and is intended to ensure that the stellar populations considered are sampled by approximately ten star particles or more. Of systems that meet the stellar mass threshold, only 5 per cent do not meet the total mass threshold of $10^8\,{\rm M}_\odot$. These systems appear to have undergone massive tidal stripping and tend to be found closer to the host halo centre, but are not numerous enough to alter the population trends explored here and in later sections.

The Auriga model seeds black holes with masses of $10^5\,{\rm M}_\odot\,h^{-1}$ in subhaloes with masses of $5 \times 10^{10}\,{\rm M}_\odot\,h^{-1}$ (Grand et al. 2017). This model results in a small population of black holes in satellite galaxies. For the subhalos that meet our resolution cuts within 1 Mpc, at redshift zero only 33 systems contain black holes (5 per cent of systems). Black holes are only found in subhaloes with final stellar masses above $10^9\,{\rm M}_\odot$ and total subhalo masses above $2 \times 10^{10}\,{\rm M}_\odot$. Subhaloes with halo masses below the halo mass limit for seeding black holes had higher halo masses in the past prior to accretion into the main host. Subhalo black holes have masses between $10^5\,{\rm M}_\odot$ and $5 \times 10^7\,{\rm M}_\odot$. At these masses, we expect feedback from these black holes to be negligible. There is one subhalo (within Au-30 at a distance of 400 kpc) that contains a $\sim 3 \times 10^8\,{\rm M}_\odot$ black hole that may contribute to the evolution of the satellite galaxy. This 'satellite' galaxy is close in size to the main halo and is not a true dwarf galaxy. There are some subhaloes with stellar and halo masses above $10^9\,{\rm M}_\odot$ and $2 \times 10^{10}\,{\rm M}_\odot$, respectively, that do not have black holes because their peak halo mass never reached the black hole seeding limit.

3.1 Luminosity distributions

Fig. 2 shows the range of mass and luminosity distributions for subhaloes within 300 kpc of the host and how this range compares to the satellite galaxy luminosity distributions found in the MW and M31 (McConnachie 2012). Note that our stellar mass limit is significantly above the stellar masses of recently discovered MW satellite galaxies found in the Dark Energy Survey (Drlica-Wagner et al. 2015; Koposov et al. 2015). The MW's satellite luminosity distribution falls within the range of the distributions produced by the 30 Auriga zoom haloes, although due to incomplete sky coverage of galactic surveys such as SDSS, the MW distribution is likely

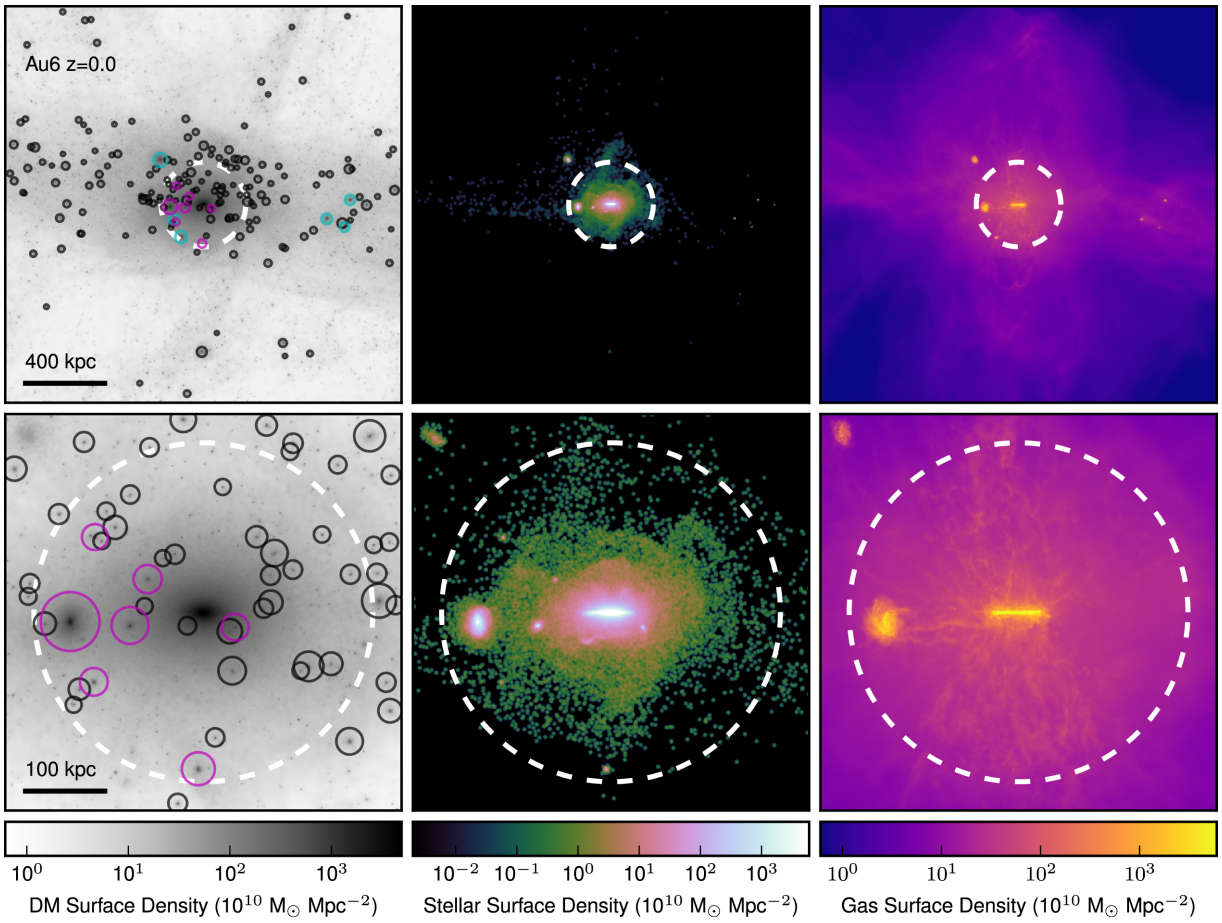

Figure 1. Projections of an example host halo (Au6) and nearby low-mass subhaloes at redshift zero. The top row shows a wide view that is 2 Mpc across; the bottom row shows a more zoomed-in view that is 500 kpc across. The depth of each projection is equal to the width. In each panel, a white dashed circle shows the R_{200} radius (214 kpc). The projections are oriented to view the disc of the host halo edge-on. The left column shows projections of dark matter density. Every subhalo with a total mass greater than 10^8 M$_\odot$ is circled. Subhaloes that have a stellar mass greater than 5×10^5 M$_\odot$ are circled in colour: magenta for subhaloes within the host R_{200}, and cyan for subhaloes beyond R_{200}. The diameter of each subhalo circle is proportional to the logarithm of the subhalo's mass. The middle column shows projections of stellar density and the right column shows projections of gas density. The zoomed-out view of the top row reveals that there is a large network of low-mass subhaloes out to large distances (∼1 Mpc) and many of these subhaloes are completely devoid of gas and stars.

incomplete at the fainter end. The distribution of M31 satellites lies at the upper number end of the simulated range. There is also a large variation in the mass and luminosity of the most massive subhalo within each host.

The total number of subhaloes within 300 kpc that have a total subhalo mass above 10^8 M$_\odot$ and a stellar mass above 5×10^5 M$_\odot$ across all 30 host halo zooms is 356; within 1 Mpc, the total is 673. There is a small population of systems that lie above the stellar mass cut but below the total halo mass cut: there are 31 of systems within 300 kpc, and within 1 Mpc, there are 35. There is significant variation in the number of subhaloes between simulated hosts. Within 300 kpc the number ranges from just 6 subhaloes (Au22) to 18 subhaloes (Au15). The average number of selected subhaloes within 300 kpc is 11.9 Again, these numbers apply to subhaloes meeting our stellar mass and total mass cuts.

Most of the subhaloes that meet the total mass cut of 10^8 M$_\odot$ do not meet the stellar mass cut of 5×10^5 and have either lower stellar masses or are completely dark. These systems are shown in the right most panel in Fig. 2. Within 300 kpc, only 20 per cent of subhaloes above 10^8 M$_\odot$ in total mass meet our stellar mass threshold and within 1 Mpc, only 10 per cent do so. Many of the systems excluded by our selection criteria are completely dark. Within 300 kpc, 70 per cent of all subhaloes with masses above 10^8 M$_\odot$ are dark and within 1 Mpc 84 per cent are dark. The most massive entirely dark system has a subhalo mass of 5.4×10^9 M$_\odot$ and all subhalos with subhalo masses above 5.6×10^9 M$_\odot$ have stellar masses above our stellar mass threshold of 5×10^5 M$_\odot$. These results, along with the subhalo mass and luminosity distributions of more luminous satellite systems shown in Fig. 2, are consistent with the findings of the APOSTLE simulations that used a different model for subgrid star formation and feedback physics and for hydrodynamics (Sawala et al. 2016b).

3.2 Gas properties

We explore the gas content of subhaloes by estimating the mass of neutral hydrogen gas within each subhalo system. Following the methods of Marinacci et al. (2017), we compute the total H I mass within each gas cell. For non-star forming cells, this mass comes directly from the fraction of neutral hydrogen given by the atomic rate equations that are solved to give non-equilibrium atomic cooling rates. For star-forming cells, we apply assumptions of the two-phase subgrid ISM model employed in the Auriga simulations, where gas in star-forming cells is assumed to be split between a

Table 1. Subhalo population properties by host halo.

Simulation	Host M_{200} (10^{12} M$_\odot$)	Host R_{200} (kpc)	$N_{\rm sub}$ (<300 kpc/1 Mpc)	max($v_{\rm max}$) (km s^{-1})	$f_{\rm quenched}$ (<300 kpc/1 Mpc)	$f_{\rm H\,I\,poor}$ (<300 kpc/1 Mpc)
Au1	0.93	206	11/30	112	0.36/0.53	0.27/0.4
Au2	1.91	262	13/25	152	0.62/0.44	0.62/0.44
Au3	1.46	239	10/14	99	0.8/0.71	0.8/0.64
Au4	1.41	236	13/31	50	0.77/0.58	0.69/0.48
Au5	1.19	223	15/19	75	0.93/0.89	0.87/0.79
Au6	1.04	214	7/13	90	0.86/0.69	0.71/0.38
Au7	1.12	219	8/13	38	0.62/0.46	0.62/0.46
Au8	1.08	216	10/26	160	0.8/0.58	0.7/0.46
Au9	1.05	214	11/16	29	1.0/0.88	1.0/0.81
Au10	1.05	214	11/18	66	0.55/0.56	0.36/0.28
Au11	1.65	249	12/22	158	0.42/0.32	0.5/0.27
Au12	1.09	217	7/14	65	0.57/0.36	0.57/0.29
Au13	1.19	223	14/27	97	0.79/0.59	0.79/0.52
Au14	1.66	249	7/17	64	0.71/0.76	0.57/0.59
Au15	1.22	225	18/21	135	0.61/0.52	0.61/0.52
Au16	1.5	241	15/30	117	0.87/0.7	0.73/0.53
Au17	1.03	213	12/17	53	0.58/0.65	0.5/0.47
Au18	1.22	225	13/44	84	0.62/0.57	0.62/0.52
Au19	1.21	225	11/18	102	0.55/0.44	0.45/0.39
Au20	1.25	227	16/30	133	0.75/0.57	0.69/0.5
Au21	1.45	239	15/31	92	0.87/0.55	0.67/0.39
Au22	0.93	205	6/8	75	0.67/0.62	0.67/0.5
Au23	1.58	245	12/17	49	0.92/0.82	0.83/0.71
Au24	1.49	241	13/37	103	0.85/0.59	0.77/0.46
Au25	1.22	225	16/23	147	0.69/0.7	0.62/0.52
Au26	1.56	245	15/29	45	0.93/0.72	0.93/0.69
Au27	1.75	254	14/20	94	0.71/0.6	0.71/0.55
Au28	1.61	247	12/25	46	0.83/0.6	0.58/0.36
Au29	1.54	244	7/13	139	0.86/0.54	0.71/0.46
Au30	1.11	218	12/25	145	0.92/0.76	0.92/0.72

Note. The quantities presented in each column are (1) the simulation name, (2) the host halo M_{200}, (3) the host halo R_{200}, (4) the number of satellites, defined as subhaloes within 300 kpc of the host halo (first number) or 1 Mpc (second number), with a minimum of stellar mass within $2r_{1/2}$ of 5×10^5 M$_\odot$, a total subhalo mass greater than 10^8 M$_\odot$, and a dark matter mass greater than 10^6 M$_\odot$, (5) the $vv_{\rm max}$ of the largest subhalo within 300 kpc, (6) the fraction of quenched subhaloes (see Section 3.3 for a description of our quenching criteria), and (7) the fraction of subhaloes that have less than 10^5 M$_\odot$ in H I mass. These simulations are the Level 4 resolution simulations from Grand et al. (2017).

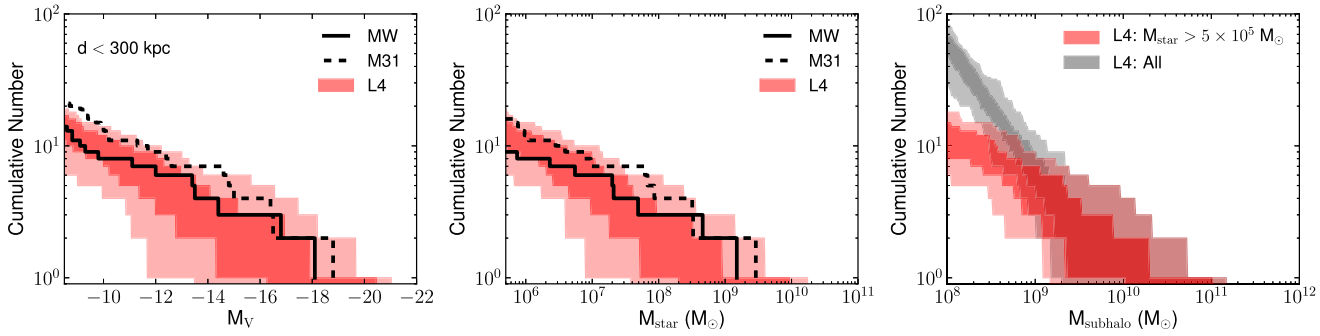

Figure 2. Cumulative distributions of satellite galaxy properties for systems within 300 kpc of each simulated host. Left: Ensemble of cumulative distributions of satellite V-band absolute magnitudes, M_V. The light red envelope encloses the individual cumulative distributions of all 30 systems in our simulated sample. The dark red envelope encloses the central-most two thirds of these distributions. The cumulative distributions of satellite galaxies within 300 kpc of the MW and M31 are also shown, calculated with data from McConnachie (2012). Middle: Ensemble of cumulative distributions of satellite stellar masses. Satellite stellar masses are taken to be the total stellar mass within $2 \times r_{1/2}$. Shaded regions have the same meaning as the left-hand panel and data for the MW and M31 are also shown. Right: Ensemble of cumulative distributions of satellite subhalo masses. The satellite subhalo masses are taken to be the total subhalo mass returned by SUBFIND for each system. The red contours enclose the cumulative distribution of all subhaloes with a stellar mass greater than 5×10^5 M$_\odot$, which is approximately the mass of 10 star particles. The grey contours enclose the cumulative distributions of all subhaloes, including subhaloes without stellar particles.

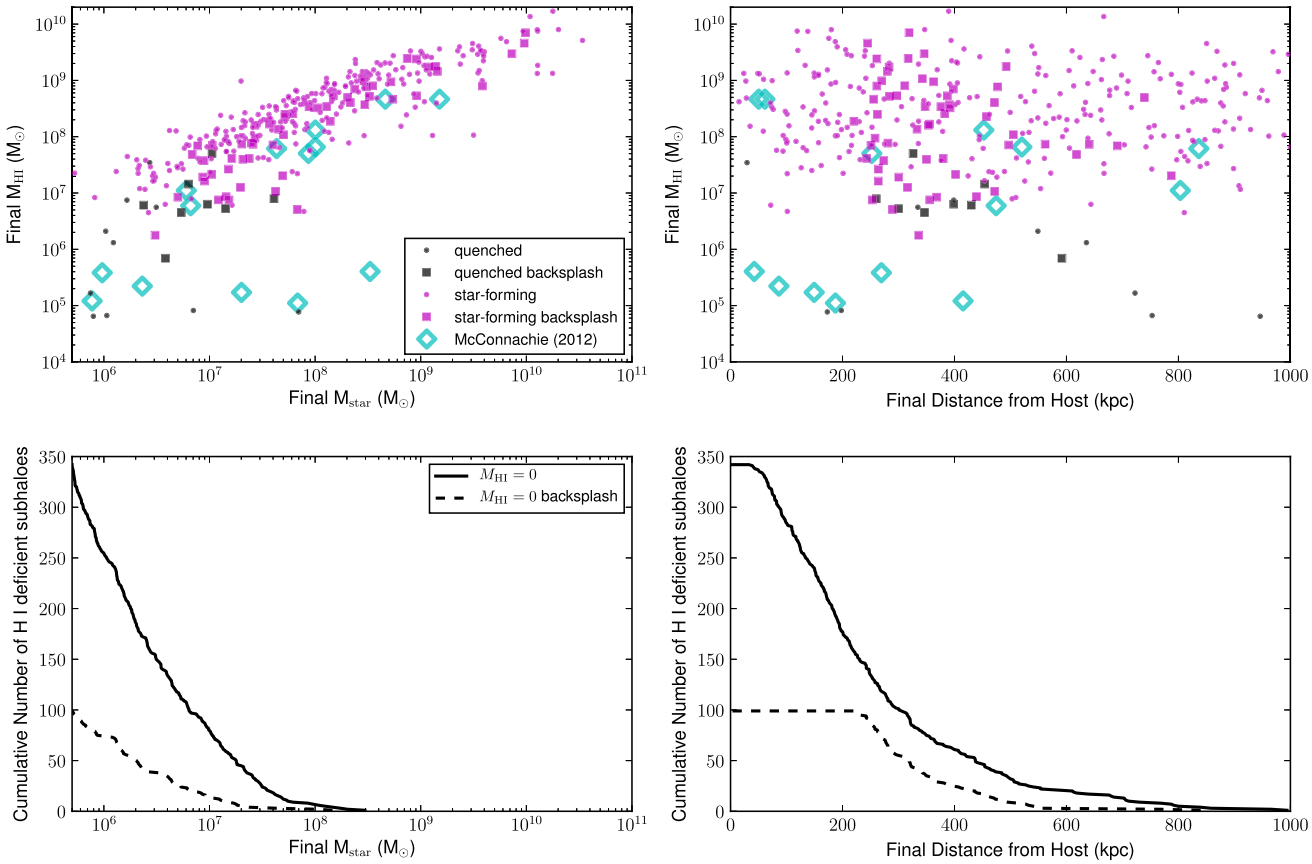

Figure 3. H I masses of subhaloes within 1 Mpc versus final stellar mass (top left) and final distance from the host (top right). All systems with non-zero H I masses are shown. Quenched systems are shown with back points and star-forming systems are shown with magenta points. 'Backsplash' systems (systems beyond R_{200} at $z = 0$ that have passed within R_{200} at some earlier redshift) are shown with squares; satellites and non-backsplash isolated systems are shown with circles. Measured H I masses of Local Group systems within 1 Mpc of either the MW or M31 (McConnachie 2012) are also shown (cyan diamonds). Systems that have zero H I masses are shown in the lower panels: cumulative distributions of the number of H I deficient systems with stellar masses greater than plotted value (left) and the number of H I deficient systems with final distances greater than the plotted value (right). Distributions for H I deficient backsplash systems are shown with dashed lines. Most H I systems have lower stellar masses and/or are closer to their host.

hot phase and a cold phase that are in pressure equilibrium and is empirically calibrated to observations of nearby galaxies (Blitz & Rosolowsky 2006; Leroy et al. 2008).

Using these H I cell masses, we compute for each subhalo a spherically averaged, radial volume density profile for the H I gas. This spherical volume density profile is then projected with the Abel transform integral to compute a radial H I column density profile for the subhalo. From this H I column density profile, the radius where the H I column density drops below 10^{20} cm^{-2} is found. The total H I mass for the subhalo is then taken to be the sum of H I cell masses of all gas cells within this computed radius. The column density 10^{20} cm^{-2} is $\sim$10 per cent of the peak column density of Leo T, one of the lowest luminosity Local Group dwarf galaxies to contain H I (Ryan-Weber et al. 2008). We found that H I system masses did not substantially increase for threshold values lower than this value.

Fig. 3 shows the H I mass of subhaloes versus their stellar mass and distance from their host. There appears to be a correlation between stellar mass and H I mass for H I-rich systems. There does appear to be a strong environmental effect as well, as shown in Fig. 4, especially for subhaloes with stellar masses below 10^8 M$_\odot$. This is consistent with the overall environmental trend found for the H I content of MW and M31 satellites (Grcevich & Putman 2009). Fig. 3 also shows that a significant fraction of isolated systems with zero H I mass are 'backsplash' systems, which we will discuss in Section 5.3. It does appear, however, that our estimate of H I mass is a factor of a few greater than in observed H I-rich systems at the same stellar mass. It is possible that this overestimate is due to unaccounted for ionizing sources (such as massive stars within the subhaloes themselves) or limitations of our ISM subgrid model. Among systems with a non-zero H I mass, there does not appear to be a correlation between final host distance and H I mass.

Despite these limitations, our estimates of the H I content do appear to be robust enough to examine general trends. We separate subhaloes into two groups: 'H I-rich' systems that have an H I mass greater than 10^5 M$_\odot$ and 'H I-poor' systems that have an H I mass less than 10^5 M$_\odot$. Most of the H I-poor systems in fact have little to no gas mass associated with them. Fig. 4 shows the fraction of H I-poor systems across the sample. For systems with stellar masses below 10^7 M$_\odot$, roughly the stellar mass of the Fornax satellite galaxy, over 80 per cent are H I poor within 300 kpc of the host. There appears to be a sharp drop in the fraction of H I-poor systems around 500 kpc. Beyond 500 kpc, less than 40 per cent of systems below 10^7 in stellar mass are H I poor.

In all distance bins, there is a strong stellar mass dependence for the H I content. Very few systems with a stellar masses above 10^8 M$_\odot$ (roughly the stellar mass of the SMC) are H I poor. The stellar mass at which virtually no system is H I-poor drops for larger distance bins; for example, systems that are more than

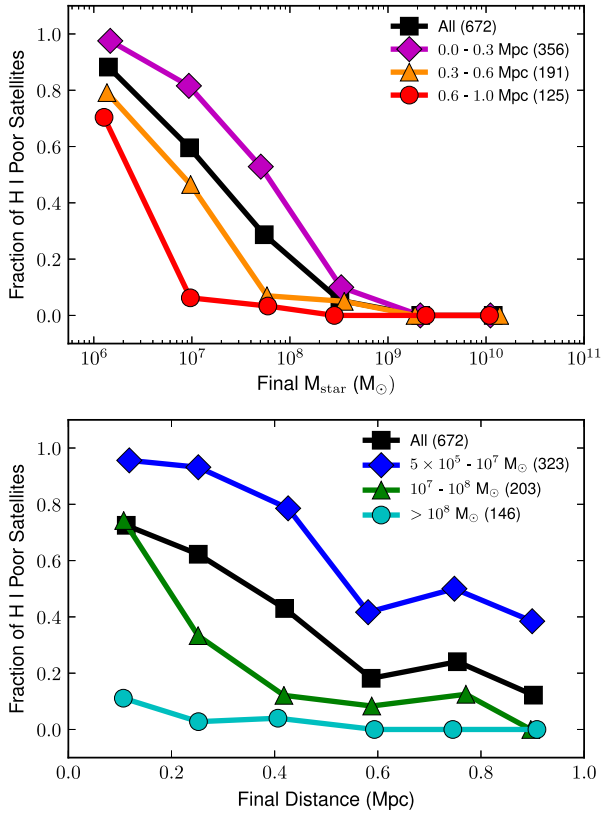

Figure 4. Top: Fraction of subhaloes with H I masses below 10^5 M$_\odot$ (called here 'H I Poor') plotted versus final stellar mass. Trends for subhaloes found in different distance ranges are plotted with different colours and symbols as labelled and the total number of subhaloes in each distance trend is indicated in parentheses after each label. Bottom: Fraction of H I-poor systems plotted versus final subhalo-host distance. Trends for subhaloes with different final stellar mass ranges are plotted with different colours and symbols as labelled and the total number of systems in each mass range is indicated in parentheses after each label.

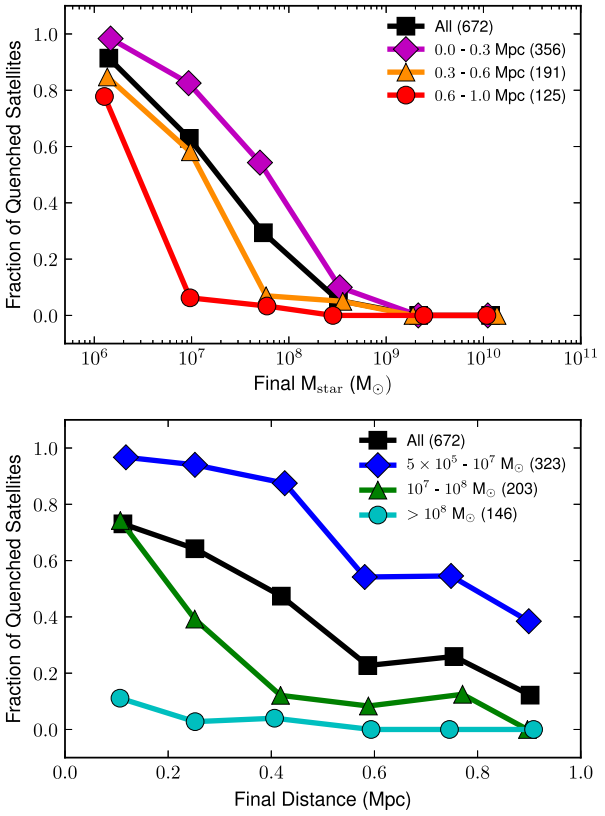

Figure 5. Top: Fraction of quenched subhaloes versus final subhalo stellar mass at redshift zero. Quenched subhaloes are defined as those whose youngest star particle is more than 100 Myr old and whose final gas phase SFR is zero. Trends for different distance bins are shown with the same bin ranges and colours as Fig. 4. The total number of satellites in each trend is labelled. Bottom: Fraction of quenched subhaloes versus final host-subhalo distance. Trends for different stellar mass bins are shown with the same bin ranges and colours as Fig. 4. The total number of satellites in each trend is labelled.

600 kpc from the host are mostly H I rich down to a stellar mass of 10^7 M$_\odot$.

3.3 Star-formation properties

The stellar mass and environmental trends seen in the H I content of subhaloes are also seen in the star-forming properties of subhaloes. Fig. 5 shows these trends, with regards to the fraction of quenched subhaloes. Here, and in subsequent analysis, we define a 'quenched' subhalo as being one whose youngest star particle is more than 100 Myr old and whose $z = 0$ star formation rate (SFR) is zero. A subhalo's SFR is computed as the sum of the SFRs of individual gas cells linked to the system by the SUBFIND algorithm.

Across the entire sample, no subhalo with a stellar mass of 10^9 M$_\odot$ or greater is quenched, regardless of environment, and most subhaloes with a stellar mass above 10^8 M$_\odot$ are also unquenched. The majority of low-mass systems ($M_{\rm star} < 10^7$ M$_\odot$) are quenched. At these masses, the fraction of quenched systems tends to be higher than the fraction of H I-poor systems. At a stellar mass of 10^6 M$_\odot$, the fraction of quenched systems is over 70 per cent regardless of distance from the host. For the most distant low-mass systems (beyond 500 kpc), less than 60 per cent are quenched, compared to less than 40 per cent being H I poor. This indicates a population of quenched subhaloes with H I masses greater than 10^5 M$_\odot$.

4 QUENCHING PROCESSES

We now discuss the physical mechanisms driving quenching in subhaloes. The evolution of the gas content of individual subhaloes is suggestive of some quenching mechanisms, such as ram pressure stripping. Fig. 6 presents the cumulative star formation histories and gas fraction evolution of several subhaloes that end the simulation within R_{200} of one of Auriga hosts. The example systems quench at a variety of lookback times ranging from more than 10 Gyr ago to less than two, and one system remains star-forming and gas rich at redshift zero. While star-forming, most satellites maintain gas fractions close to 0.1. When they lose gas, many systems do so rapidly, and once lost, none of these example systems recover their gas. This rapid drop in the central gas fraction may be a signature of ram pressure stripping of the subhalo gas.

The spatial distribution of subhaloes beyond R_{200} (Fig. 1) is also suggestive of larger-scale environmental effects. Many subhaloes appear to be accreted into the host halo environment from large-scale filaments that have their own associated gas reservoirs and contain many other subhaloes, which may both play a role in the baryon histories of systems. The impact of feedback in our model should also be considered and effects from the cosmic UV background may also play a role.

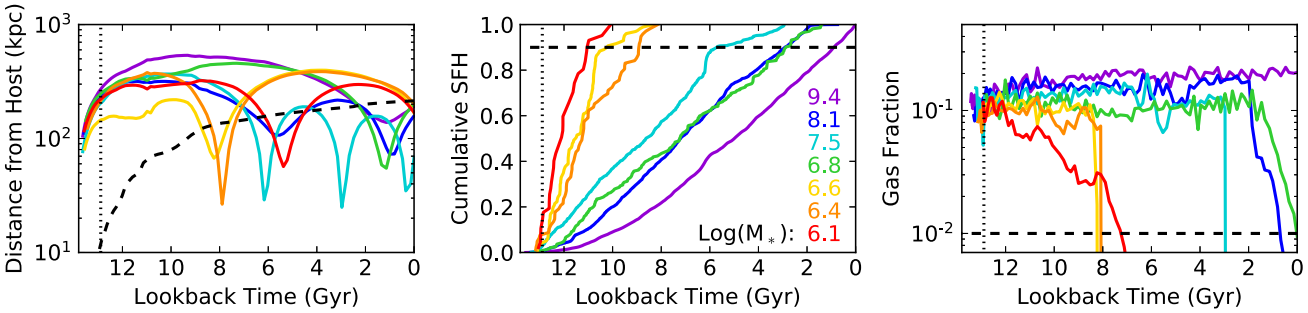

Figure 6. Evolution of luminous satellites of Au6. The plotted satellites all end the simulation within R_{200}, have a minimum final subhalo mass of 10^8 M$_\odot$, and a minimum stellar mass within $2 \times r_{1/2}$ of 5×10^5 M$_\odot$. The vertical dotted line in each panel marks $z = 6$, the time when reionization concludes. Left: Distance in physical kpc between the host halo and the satellite halo versus lookback time. Each subhalo is plotted as a differently coloured line; the R_{200} radius of the host halo (which evolves with time) is plotted with a black dashed line. Middle: Cumulative star formation history of star particles that end the simulation within $2 \times r_{1/2}$ versus lookback time. For reference, a threshold value of 0.9 is indicated with a black dashed line. The logarithm of the final stellar mass of each system is indicated in the corresponding colour. Right: Satellite gas fraction (gas mass divided by the total mass) within $2 \times r_{1/2}$ versus lookback time. For reference, a threshold value of 0.01 is indicated with a black dashed line.

4.1 Ram pressure stripping

We begin with an examination of ram pressure stripping to determine whether it is responsible for the rapid drops in gas content that many subhaloes exhibit when they are accreted into the host halo as seen in this study and others (e.g. Okamoto & Frenk 2009). Ram pressure stripping refers to the phenomenon that occurs when the pressure exerted on a galaxy's internal gas by its motion through an ambient medium (such as the CGM or the ISM) overcomes the gravity exerted by stars and dark matter within the galaxy on the gas (Gunn & Gott 1972), resulting in a stripping of the internal gas from the galaxy in motion.

The ram pressure felt by a satellite's gas is $P_{\rm ram} = \rho_{\rm CGM} v_{\rm sat}^2$, where $\rho_{\rm CGM}$ is the density of the medium though which the satellite galaxy is moving and $vv_{\rm sat}$ is the relative velocity of the satellite to the surrounding gas. The restoring force per area on the satellite's gas can be expressed as $P_{\rm rest} = |\frac{\partial \Phi}{\partial z_h}|_{\rm max} \Sigma_{\rm gas}$, where $\Sigma_{\rm gas}$ is the satellite's gas surface density, z_h is the direction of motion (and gas displacement), Φ is the gravitational potential, and $|\frac{\partial \Phi}{\partial z_h}|_{\rm max}$ is the maximum of the derivative of Φ along z_h (Roediger & Hensler 2005).

Using the merger trees, we have estimated for each satellite the ram pressure and restoring force felt by its internal gas over its history. For the quantity $vv_{\rm sat}$, we adopt the velocity of the subhalo relative to the host halo's velocity. For the quantity $\rho_{\rm CGM}$, we compute an average radial gas density profile extending out to a radius of $4R_{200}$ for the host halo in each snapshot. The quantity $\rho_{\rm CGM}$ is then interpolated from this average gas density profile in the corresponding snapshot at the subhalo's radial position. The average radial gas density profile is computed over all gas cells belonging to the host's primary subhalo and unlinked cells (cells that do not belong to any halo or subhalo). The values for $P_{\rm ram}$ that we compute from these two values will in many cases not capture the maximum ram pressure felt at pericentric passages because the spacing of our outputs is not sufficient to capture the true pericentric distance for many orbits.

Satellites in Auriga encounter many local perturbations in the density and velocity fields of the gas that they encounter along their orbital path. These variations arise from feedback-driven winds from the host galaxy, clumpy gas accretion from the IGM, and stripped gas from other satellites. Our strategy for estimating the ram pressure felt by satellites neglects these local variations, however, with the refinement strategy adopted in the Auriga simulations, gas at lower densities (as found in the outskirts of the host haloes) is resolved with fewer resolution elements. This is a result of the simulations' Lagrangian refinement strategy that ensures an approximately constant gas cell mass throughout the simulation. The median cell diameter of star-forming gas in the host discs is approximately 300 pc, but beyond 10 per cent of R_{200} cells typically have a diameter greater than 1 kpc. An estimate of the local ram pressure would, at large distances, involve averages over small numbers of cells and be sensitive to computational choices. Our radially averaged estimate, while neglecting local effects, robustly captures the effect of radial infall that drives the main change in ram pressure, which can vary by orders of magnitude.

The restoring force estimates often assume a disc configuration for the galaxy within a spherical halo (Gunn & Gott 1972; Roediger & Hensler 2005), which is the case for some systems in our sample, but not the case for others. We therefore adopt a simple estimate for $\Sigma_{\rm gas}$ and $|\frac{\partial \Phi}{\partial z_h}|_{\rm max}$ that can be applied to all systems in the sample uniformly. The gas surface density is estimated from the radius enclosing half the gas mass ($r_{1/2}^{\rm gas}$), such that $\Sigma_{\rm gas} = M_{\rm gas}/2\pi(r_{1/2}^{\rm gas})^2$ (where $M_{\rm gas}$ is the total mass in gas). We estimate $|\frac{\partial \Phi}{\partial z_h}|_{\rm max} \sim v_{\rm max}^2/r_{\rm max}$, where $vv_{\rm max}$ is the maximum velocity of the spherically averaged subhalo rotation curve and $r_{\rm max}$ is the radius where this peak occurs.

Our simulations' ability to capture the restoring force depends in part on the accuracy of our gravity calculation. The minimum softening length used is more than 300 pc in these simulations and the typical half-light radius of observed systems at our lower luminosity limit is close to this value. (We also note that gas cells can and do have radii smaller than the minimum softening length in dense gas.) We find typical half stellar mass spherical radii of approximately 1–2 kpc; however, we have not attempted to model properly the shapes of the satellite systems, which is typically done for observed systems. Many of our systems are very squashed or have stellar discs, and the spherical radii are overestimates for this reason.

When examining the dynamical mass within 300 pc, we find values between 10^6 M$_\odot$ and 10^7 M$_\odot$ for systems with stellar masses up to 10^7 M$_\odot$, with our higher resolution simulations being slightly closer to 10^7 M$_\odot$. This is consistent with observed systems (Strigari et al. 2008). We also find small differences in both these quantities with our high-resolution simulations (described in the Appendix)

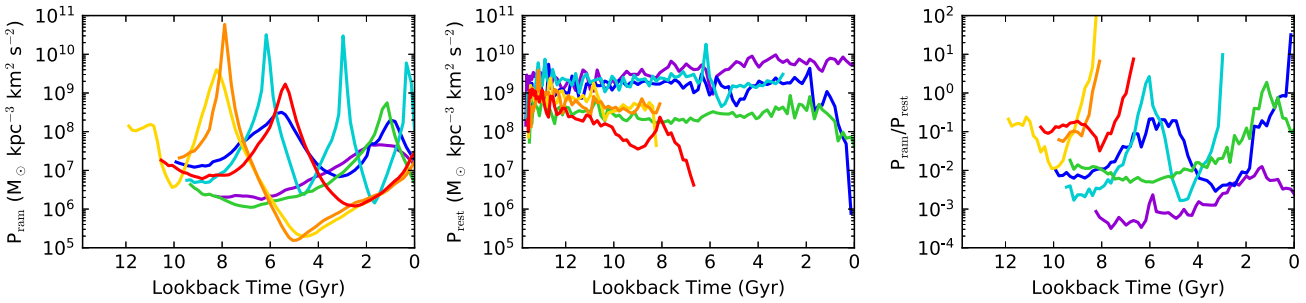

Figure 7. Evolution of pressure forces felt by gas in the luminous satellites of Au6. Satellites plotted end the simulation within R_{200} and are the same as those plotted in Fig. 6 with the same colours. Left: Estimate of the ram pressure felt by satellites versus lookback time as computed from a time-dependent average gas density profile of the host and the satellites own velocity. Each line begins when the satellite comes within $4R_{200}$ of the host. Middle: Estimate of the restoring force per area felt by gas within each satellite. Each line begins when the satellite first forms stars and ends once the satellite's gas mass falls to zero. Note that following Newton's gravitational law, the force between a subhalo's stars and gas is only non-zero when the mass of both stars and gas within the subhalo is non-zero. Right: Ratio of the ram pressure to the restoring force per area plotted in the first two panels. Each line begins and ends when either P_{ram} or P_{rest} is undefined.

that have a factor of 2 better softening lengths. We conclude that we are capturing the central potentials of these systems reasonably well for the purposes of this study, but defer a fuller discussion of the internal structure of these objects to a study of our higher resolution simulations.

Fig. 7 shows the evolution of the ram pressure and restoring force felt by satellites over their histories. Fig. 7 can be compared to Fig. 6, which depicts the same satellites, and it can be seen that sharp increases in the ratio P_{ram}/P_{rest}, rising above 1, correspond in most cases to a sudden, sharp drop in the gas fraction.

There are a few interesting cases among this group of satellites. The system plotted in dark blue in Figs 6 and 7 appears to have a sharp drop in its gas fraction that does not quite match in time its sudden increase in the P_{ram}/P_{rest} ratio. A closer examination of this system revealed that the drop in the gas fraction is due to an interaction with another satellite (in fact, the purple satellite) that is more massive and gas rich. The gas loss does appear to be due to ram pressure, but instead from the gas disc of this secondary satellite rather than from the host's gas. Our estimate for P_{ram} from an average gas density profile is inaccurate in a case like this.

The system plotted in light blue has a complicated orbital history that includes three pericentric passages. All three of these pericentric passages correspond to a spike in the ram pressure, but during the first pericentric passage, the restoring force of the system is great enough to counter the ram pressure. What occurs instead is a compression of gas within the satellite resulting in a small starburst (apparent in the cumulative star formation history in Fig. 6). However, the result of this starburst is to lower the restoring force of the satellite (perhaps due to feedback effects associated with the starburst). On the subsequent pericentric passage, the ram pressure is able to overcome the now lower restoring force, resulting in a complete stripping of gas from the subhalo.

A visual example from our resimulation of Au6 with an increased number of outputs is shown in Fig. 8. Here, a satellite that ends the simulation within R_{200} and with a stellar mass of $6.3 \times 10^6\,M_\odot$ is shown during a low-redshift stripping event. Even before this system crosses R_{200}, it appears to already have a low-density gas tail. As the system moves towards pericentre, a more pronounced gas tail forms and the gas within the centre of the halo appears to form a contact discontinuity surrounded by a weak bow shock. The edges of this structure are eroded and a small bullet-like clump of gas remains, until it too is eroded, and all the gas is stripped from the subhalo. This system's stellar mass does not change appreciably during this event.

In Fig. 9, we present the effect of ram pressure on the satellite sample as a whole for systems within R_{200} at $z = 0$. Here, we identify the maximum in the ratio P_{ram}/P_{rest} over the history of each satellite. We examine the correlation of this ratio with the final stellar mass of the system and the change in gas mass at the time of the ratio peak. The peaks in P_{ram} are likely lower limits to the true peak values because of the cadence in our outputs and the very steep rate of change in this value.

A majority of unquenched systems do not reach values in P_{ram}/P_{rest} above 1 (∼29 per cent do so) and most do not reach values above 10 (only ∼5 per cent). Among quenched systems, most reach P_{ram}/P_{rest} ratios above 1 (∼95 per cent) and the fractional change in gas mass between the snapshot before the peak P_{ram}/P_{rest} and the snapshot after is nearly 100 per cent for over 70 per cent of quenched systems. What this gas loss means for the star formation histories of these systems likely varies; for systems that quench before infall, they may have already been quenched, and for the systems that form stars after this gas stripping event occurs, they may reaccrete gas and have later epochs of star formation.

4.2 Tidal effects and starvation

As we will discuss in later sections, about half of quenched systems in our satellite sample quench either significantly before or significantly after first falling into their host halo, indicating a role for quenching mechanisms other than ram pressure stripping. Most of the systems that quench after infall are higher mass. High-mass systems that quench significantly after first infall may be thought of as an extension of the unquenched population that have simply had enough time to cease star formation, given the longer quenching time needed in higher-mass systems. Indeed, all of the late, high-mass quenchers appear to have had an interaction with the host halo prior to 6 Gyr ago.

Investigating some of the high mass, late quenchers reveals that a number of them show a slow-down in their SFR after accretion into the host. These systems are few in number, so it is difficult to determine population wide statistics. They appear to have orbits with large angular momenta that prevent close pericentric passages, but do in the end undergo a final ram pressure stripping event after a long period of star formation slowdown. When the slowdown occurs, the

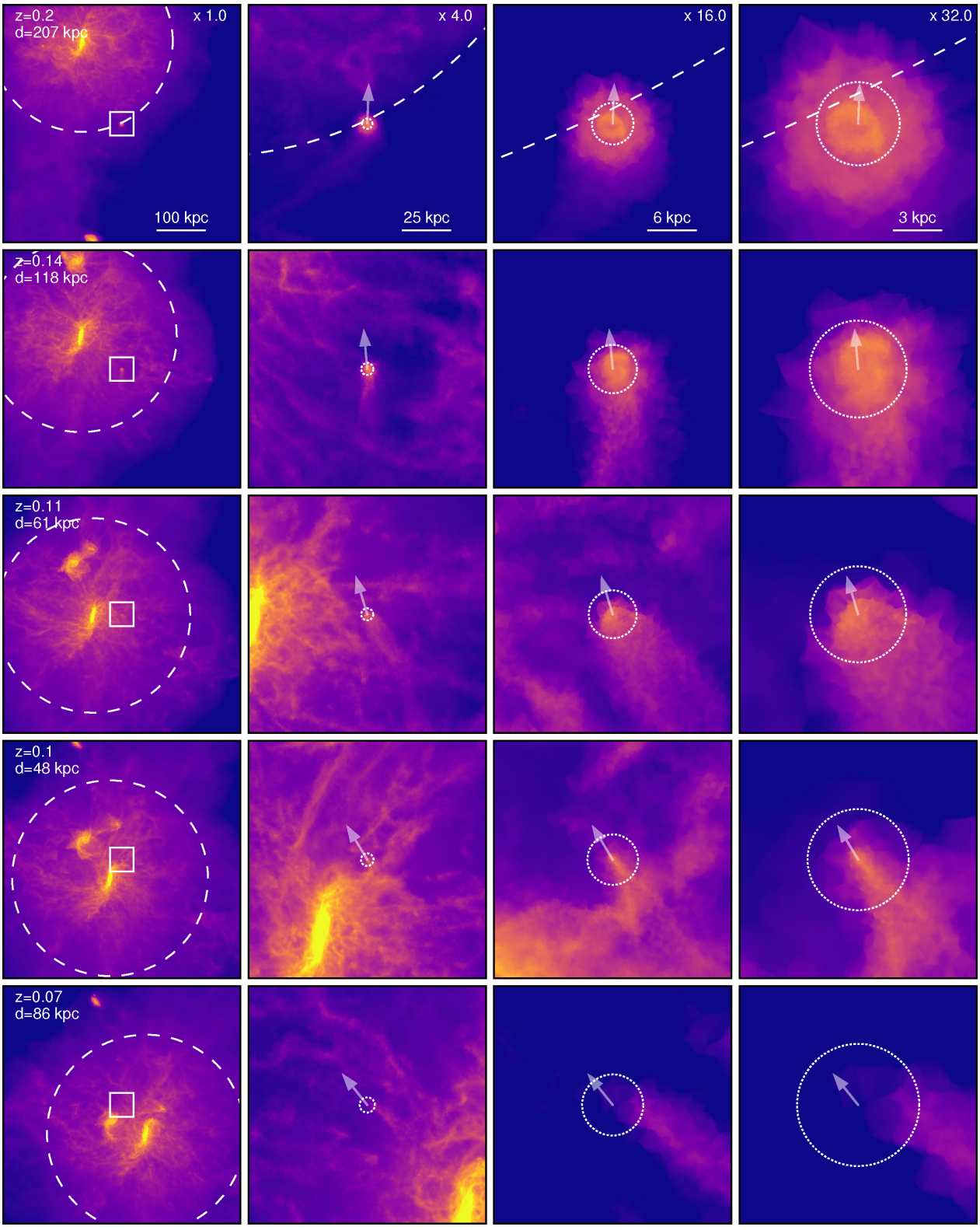

Figure 8. Gas density projections of an individual subhalo, as it falls into the host halo and is ram pressure stripped. Each row shows the subhalo at a single time and each column shows projections through cubes of decreasing volume from left to right. The projection cube length decreases by the factor indicated for each column and are, from left to right, 500, 125, 31, and 16 kpc. In the left most column, the subhalo is surrounded by a 50 kpc square. In the other three columns, the subhalo is surrounded by a dotted-white circle that has a radius equal to twice the half-stellar mass radius. The direction of the subhalo's velocity in the plane of the image is shown with an arrow. The host halo's R_{200} radius is indicated by a dashed white circle. The redshift and the host-subhalo distance are indicated in each row. These images show an example subhalo from a resimulation of Au6 that was run with eight times more snapshots. The subhalo does not reaccrete gas after this stripping event and ends the simulation composed only of stars and dark matter.

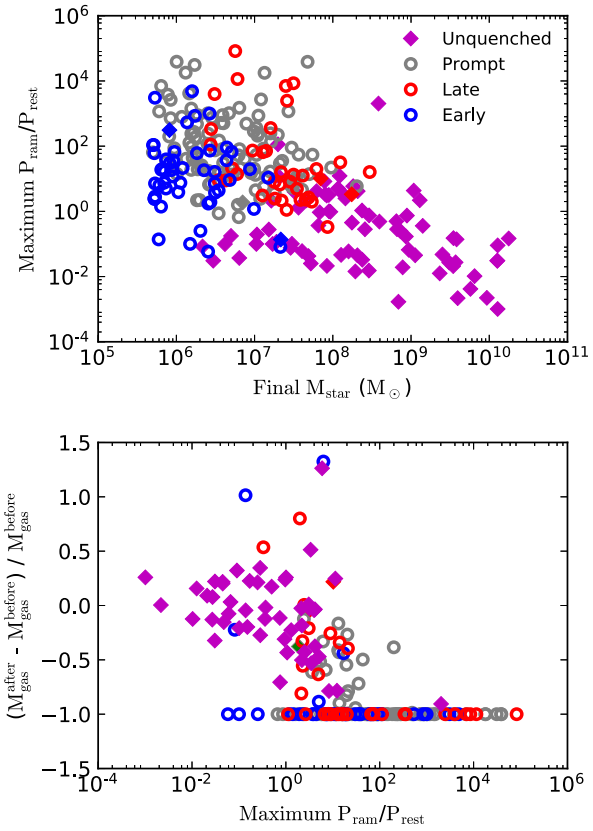

Figure 9. Top: The peak value in the ratio $P_{\rm ram}/P_{\rm rest}$ felt by each satellite system that ends the simulation within R_{200} of its host. Systems where the maximum value occurs in the final snapshot are not included as well as systems where $P_{\rm ram}/P_{\rm rest}$ is undefined (mainly systems that lose their gas prior to coming within $4R_{200}$ of the host). Open circles show systems with no gas and solid diamonds show systems with a non-zero final gas mass. Magenta points are unquenched systems; other colours indicate the system's membership in the quenching samples described in Section 5.2. Bottom: The fractional change in gas mass of satellite systems between the snapshot directly before the peak $P_{\rm ram}/P_{\rm rest}$ ratio occurs and the snapshot directly after. Symbol styles and colours have the same meaning as the top panel.

total gas depletion time (the gas mass divided by the SFR) in these systems actually goes up because the SFR drops faster than the gas mass. This is somewhat different from the classical starvation quenching picture, but may be due to our model's ISM treatment.

Tidal effects may play a role in quenching these systems; however, these effects would need to act faster than ram pressure, but at the same time, be slow enough to produce quenching before complete destruction of the subhalo. Higher-mass systems that are able to resist the effects of ram pressure for a longer period of time are candidates for this process. Fig. 10 shows that many systems in our sample have lost a substantial fraction (>80 per cent) of their peak halo mass by $z = 0$ and have large stellar masses for their halo masses as compared to trends from abundance matching studies (Guo et al. 2010; Behroozi et al. 2013) and the cosmic baryon fraction (Ω_b/Ω_m).

Recent idealized simulations by Safarzadeh & Scannapieco (2017) suggest that ram pressure stripping and tidal stripping are interrelated processes in low-mass, gas-rich systems; when gas is stripped from gas-rich satellites, they find this sudden change in the satellite's central potential can impact orbits of stars within the system and enhance tidal stripping.

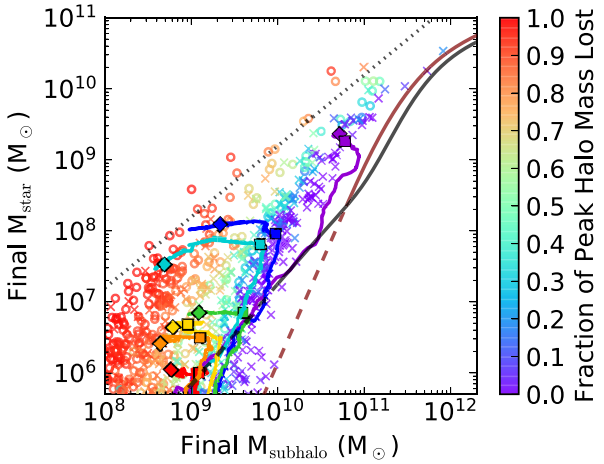

Figure 10. The final stellar mass versus final halo mass for all resolved systems within 1 Mpc of the host galaxies in all 30 Auriga simulations. Open circles are systems within R_{200} at $z = 0$ and *x*s are systems beyond R_{200}. The colour of these points indicate the fraction of their total halo mass that has been lost from their peak mass as measured from their merger trees: red points have lost over 90 per cent of their halo mass and purple points have lost very little mass. Coloured lines show the evolutionary tracks of a few example systems from Au6 in this plane. Along these tracks, squares indicate the point at which the system first crosses within R_{200} and diamonds indicate their final position. The black dotted line indicates the cosmic baryon fraction Ω_b/Ω_m. The brown solid/ dashed line indicates an abundance matching estimate for central dark matter haloes taken from Guo et al. (2010) and the black solid/dashed line indicates an estimate from Behroozi, Wechsler & Conroy (2013). For both these trends, the solid portion of the line covers the portion of parameter space where these studies make predictions and the dashed lines are power-law extensions of the estimated trends to lower masses.

The evolution of some example systems in Fig. 10 shows that the subhalo mass of these systems can drop by several factors before the stellar mass is affected. In some more massive systems, there is a modest increase in stellar mass post first infall. Indeed, there is very little negative change seen in the stellar mass of tidally affected satellites. This is probably due to the high concentration of the stellar component compared to the dark matter, and it is likely that once the stellar component of the subhalo is tidally affected, the time-scale for the subhalo destruction is short. The main effect of tides on the star formation histories of satellites in our model is therefore most likely the suppression of gas accretion, which will starve systems and will increase the effectiveness of other mechanisms, such as ram pressure stripping or stellar feedback.

4.3 Field quenching and low-mass systems

The quenching trend with mass for isolated systems demonstrates a sharp increase in quenched fractions below $M_{\rm star} = 10^7\,{\rm M}_\odot$. This indicates a field quenching mechanism that is effective in quenching low-mass systems. This mechanism appears to operate in our higher-resolution simulations (see the Appendix), which rules out resolution quenching. It is also notable that systems beyond R_{200} that have never had an interaction with a host halo demonstrate a very strong mass-dependent quenching signal (as shown in Fig. 14) that indicates that a 'backsplash' population cannot be the sole explanation.

Low-mass systems that quench before first infall appear to accrete into the host haloes at a steady rate across the sample (as shown by the satellite-host infall times shown in Fig. 11 and discussed in

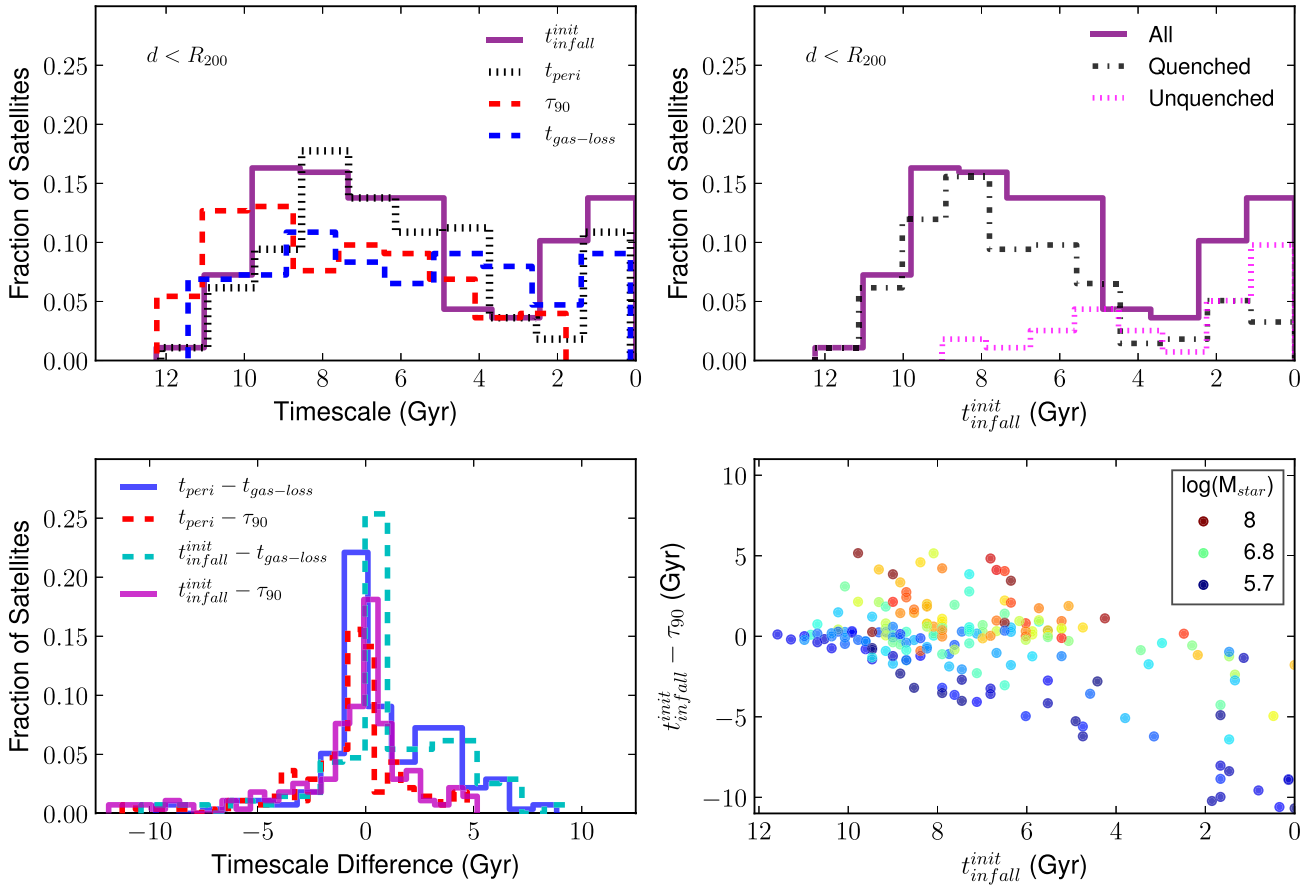

Figure 11. Distributions of evolutionary time-scales (as described in Section 5) for satellites that lie within R_{200} at redshift zero in all 30 simulations. All time-scales are measured as lookback times, where 0 is the present-day and larger time-scales correspond to higher redshift. Top left: Distributions of $t_{\rm infall}^{\rm init}$, $t_{\rm peri}$, $t_{\rm gas\text{-}loss}$, and τ_{90}. The distributions plotted are the frequency of satellites in each bin divided by the total number of satellites within R_{200}. Top right: Distributions of $t_{\rm infall}^{\rm init}$ for all systems within R_{200} and systems that are quenched and unquenched. Bottom left: Distributions of time-scale differences. Plotted here are the differences ($t_{\rm peri} - t_{\rm gas\text{-}loss}$), ($t_{\rm peri} - \tau_{90}$), ($t_{\rm infall}^{\rm init} - t_{\rm gas\text{-}loss}$), and ($t_{\rm infall}^{\rm init} - \tau_{90}$); the median values of each distribution (in the same order) are 0.1, −0.3, 0.6, and 0.0 Gyr. In distributions involving τ_{90}, only quenched systems are included. Negative numbers indicate quenching or gas loss before the orbital time-scale under comparison. Bottom right: The difference $t_{\rm infall}^{\rm init} - \tau_{90}$ plotted versus $t_{\rm infall}^{\rm init}$ for quenched systems. The colour of each point indicates its final stellar mass: blue points are low mass and red points are high mass.

Section 5). Each of these systems has a unique history and likely multiple quenching processes are at play across the sample, but these results implicate either internal processes like feedback, or global processes, such as reionization, both of which operate independently of the host galaxies in Auriga.

Stellar feedback may impact the quenching of dwarf galaxies through the generation of galactic winds that expel gas. Fig. 6 shows that baryon evolution of satellites in our sample is relatively smooth in the absence of external effects. There are few examples of gas loss and reaccretion across the entire satellite sample, which would be a possible signature of feedback effects. Some small starbursts are apparent, but appear to be correlated with pericentric passages. This lack of burstiness is in contrast to high-resolution simulations of dwarf galaxies that model the ISM self-consistently and the launching of galactic winds from local feedback processes (e.g. Fitts et al. 2017).

The feedback model employed here maintains a steady central gas fraction of 10–20 per cent (relative to the total mass) in equilibrium with gas accretion, but does not appear to expel large amounts of gas from subhaloes. It is possible that a feedback model that includes the dynamical impact of stellar feedback on the ISM would result in a more bursty star formation history and a different mass loading for galactic winds in dwarf systems. This effect could alter feedback-driven quenching. It is also possible that feedback-driven quenching is more effective at stellar masses below our threshold.

A quenching mechanism commonly appealed to in low luminosity Local Group dwarf galaxies is the effect of reionization. The filtering halo mass for the effect of reionization is often assumed to be around 10^9 $M_\odot$ because the virial temperature of haloes at this mass is similar to the IGM temperature (Gnedin 2000; Hoeft et al. 2006; Okamoto, Gao & Theuns 2008). Studies of cosmologically isolated systems at this halo mass have demonstrated the photoevaporation of gas during reionization and the subsequent suppression of post-reionization gas accretion (Sawala et al. 2010; Simpson et al. 2013; Shen et al. 2014).

The sample of systems considered here spans this filtering halo mass transition, and indeed, Fig. 1 demonstrates that there are many dark subhaloes in our simulations and star formation in many of these systems is likely suppressed by reionization. In terms of reionization fossils, i.e. luminous systems that have been quenched by reionization, the inclusion of a stellar mass threshold in our selection criteria preferentially selected systems that assembled early. Fig. 2 demonstrates that there are many more dark and underluminous subhaloes (systems with $M_{\rm star} < 5 \times 10^5$ $M_\odot$) in our simulations

above our halo mass limit. Most of the systems in our sample already had halo masses above 10^8 M$_\odot$ at $z = 6$, and in fact many lower-mass systems in our sample were of a much higher mass at $z = 6$ and subsequently lost dark matter mass by means of tidal stripping. It is likely that the stellar mass of reionization fossils with the baryonic physics model employed in the Auriga simulations falls below our stellar mass limit.

To better understand the impact of stellar feedback and reionization on quenching with the Auriga physical model, higher resolution simulations are needed, since in our current simulations, these effects likely only play an important role at stellar masses below our stellar mass threshold of 5×10^5 M$_\odot$, or approximately the mass of 10 star particles. It is also necessary to have higher snapshot cadence at the epoch of reionization (in our model $z = 6$) than our current simulations to capture the dynamics of photoevaporative winds. Simulations with an alternate, or no, UV background and also be informative in determine the impact of reionization (Simpson et al. 2013).

An alternate explanation for early, low-mass-quenched systems in our sample is environmental quenching outside the main host. This type of quenching may be a form of ram pressure quenching, where the ram pressure arises from filament gas (Benítez-Llambay et al. 2013) or gas of other subhaloes, rather than gas associated with the host halo. This type of ram pressure stripping is not captured by our estimates presented in Section 4.1 for host halo ram pressure quenching. Visual inspection of some individual systems shows filament stripping to be present with a somewhat different signature than host stripping that occurs at pericentric passages. For example, in Fig. 6, the system plotted in red appears to be a case of cosmic web quenching. The system in question crosses a filament feeding the host transversely and this interaction with the filament gas results in a partial stripping of the subhalo that quenches star formation.

Another possible effect is simple starvation. Fig. 6 shows that star-forming satellites maintain a roughly constant central gas fraction while the SFR is constant, indicating the replenishment of the gas supply. Environmental effects that interrupt this supply could cause quenching. The source of this gas supply is likely filamentary gas, and therefore, the filament environment could affect the star formation history of satellites.

5 WHEN DO SATELLITES QUENCH?

Having established trends in gas content and star formation for subhaloes in our sample at redshift zero in addition to exploring various quenching mechanisms, we will now quantify time-scales for quenching and gas loss for individual subhaloes and quantify the ensemble of these time-scales. We measure time-scales on a lookback time-scale, where 0 Gyr is the present day and larger times correspond to higher redshift.

5.1 Time-scale definitions

First, we define a quenching time-scale, τ_{90}, following the observational definition of Weisz et al. (2015). All linked star particles that end the simulation within twice the satellite's half stellar mass radius ($r_{1/2}$) are used to determine a cumulative star formation history for the system using star particles ages. From this history, τ_{90} is defined as the lookback time when 90 per cent of the satellite's final stellar mass had been formed. Note that we will apply this time-scale to both quenched and unquenched systems.

Secondly, we define a time-scale for gas loss of gas-poor satellites, $t_{\rm gas\text{-}loss}$. This time-scale relies on the merger trees to track the gas content of each system's most massive progenitor at each snapshot backwards in time. We define the gas fraction as the fraction of gas mass to total mass (gas, stars, dark matter, and black holes) within $2r_{1/2}$ and $t_{\rm gas\text{-}loss}$ as the lookback time when this gas fraction drops below 0.01 and remains suppressed below 0.01 down to redshift zero.

Fig. 6 showed the evolution of the baryon content of some example satellite systems. Also shown in Fig. 6 is the distance between the example systems and their host galaxy. These systems have a variety of orbital histories, with some systems undergoing multiple pericentric passages, while others fall in relatively late. Overall, the baryon histories of these systems appear to be highly correlated with their orbital histories, in that the times of star formation quenching, final gas loss, and crossing the host R_{200} coincide for many of the systems.

To explore these correlations, we use the merger trees to quantify a time-scale for initial satellite infall, $t_{\rm infall}^{\rm init}$, by computing the first time a satellite crosses within the host halo's R_{200} radius. Note that R_{200} changes with time. We also define a time-scale for the first pericentric passage of each satellite, $t_{\rm peri}$, which is the time of the earliest local minimum of the satellite-host distance occurring within R_{200}. Because of discrete time sampling, $t_{\rm peri}$ can be over- or underestimated. If a subhalo never comes within R_{200}, it is not assigned a quantity for these time-scales. It is the case, however, that many systems beyond R_{200} at $z = 0$ have at some point in the past come within R_{200} and therefore can be assigned values for $t_{\rm infall}^{\rm init}$ and $t_{\rm peri}$. As can be seen in Fig. 6 many systems have complex infall histories and we will explore this in more detail in Section 5.3.

5.2 Evolution of satellite systems

Fig. 11 shows the distributions of these time-scales for satellites within R_{200} and how well they coincide with each other for individual systems. First, it is apparent that the distributions of $t_{\rm infall}^{\rm init}$ and $t_{\rm peri}$ are bi-modal, as is $t_{\rm gas\text{-}loss}$ to a somewhat lesser degree. The reason for this is discussed in Section 5.3. Secondly, it is apparent that $t_{\rm gas\text{-}loss}$ and τ_{90} strongly coincide with $t_{\rm infall}^{\rm init}$ and $t_{\rm peri}$. Of quenched subhaloes, 51 per cent quenched within 1 Gyr of first infall and 48 per cent quenched within 1 Gyr of their first pericentric passage. Of gas-poor subhaloes, 43 per cent lost their gas within 1 Gyr of first infall and 45 per cent lost their gas within 1 Gyr of their first pericentric passage. On average, total gas loss occurs 1.9 Gyr after the cessation of star formation as quantified by $t_{\rm gas\text{-}loss}$ and τ_{90} for quenched and gas-poor subhaloes.

Separating systems by their quenched state, also shown in Fig. 11, shows that on average, quenched systems tend to have earlier infall times. Unquenched systems, while less numerous overall, comprise a larger portion of the late-infall systems.

There are of course many quenched systems, 49 per cent, that do not quench within 1 Gyr of first infall. Fig. 11 shows that systems that quench before first infall tend to be lower mass and systems that quench after first infall tend to be higher mass.

Examining Fig. 6, a few examples of these types are apparent. A lower luminosity system plotted in red appears to have a rapid cessation of star formation that occurs several Gyrs before its first infall into the host and then a more gradual loss of its gas mass that also appears to occur before its first pericentric passage. There is a system plotted in dark blue that appears to quench over 2 Gyr after its first infall and pericentric passage. There are also examples of systems (plotted in yellow and orange) that appear to quench close to their first infall and pericentric passages.

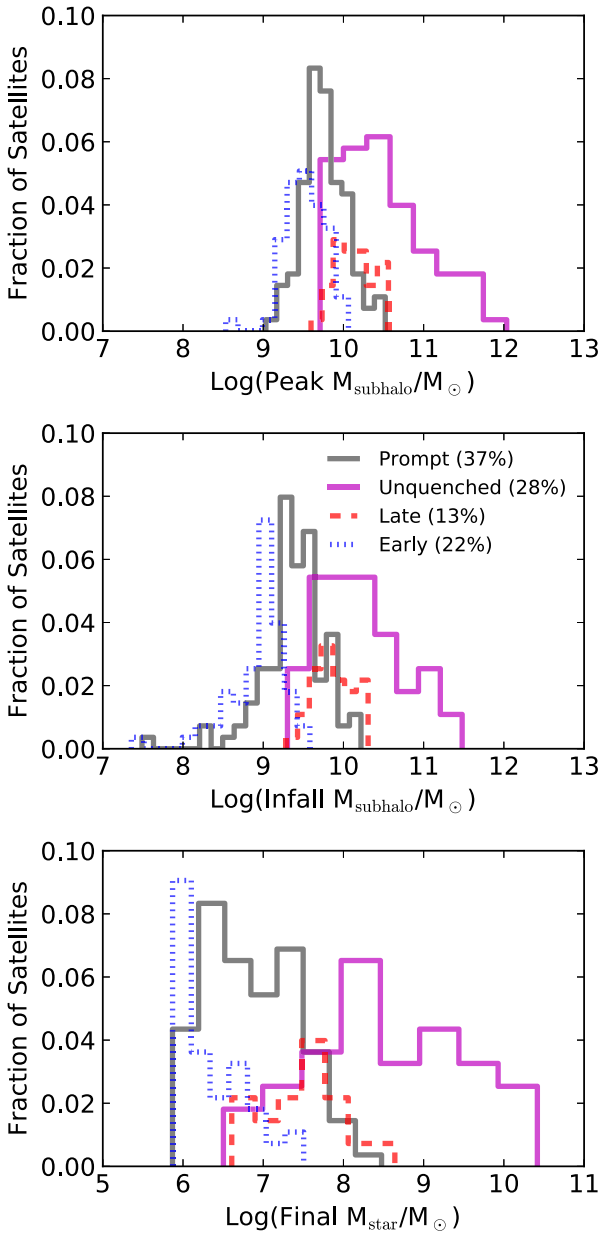

Figure 12. Properties of prompt, early, and late quenching satellites, as well as unquenched satellites, that end the simulation within R_{200}. The percentage of systems in each category is indicated, along with the line style for each distribution. Top: Distribution of the peak subhalo mass in the merger tree history of each subhalo. The fraction shown is the number frequency within each bin divided by the total number of subhaloes (673). Middle: Distribution of the subhalo mass at first infall ($t_{\rm infall}^{\rm init}$). Bottom: Distribution of satellites' final stellar mass.

To better understand these systems and examine their properties, we divide them into three categories: prompt quenchers that quench within 1 Gyr of first infall ($|t_{\rm infall}^{\rm init} - \tau_{90}| < 1$ Gyr), early quenchers that quench more than 1 Gyr before first infall ($t_{\rm infall}^{\rm init} - \tau_{90} < -1$ Gyr), and late quenchers that quench more than 1 Gyr after first infall ($t_{\rm infall}^{\rm init} - \tau_{90} > 1$ Gyr). We also consider the population of unquenched systems.

Fig. 12 shows mass distributions for these four categories of satellites. In general, unquenched systems occupy larger mass dark matter haloes than quenched systems and are more luminous. It is also the case that the mean subhalo mass (either at infall or at the peak of the subhalo's history) for late quenchers is greater than that of prompt quenchers, and the mean mass of prompt quenchers is greater than that of the early quenchers. Despite this, there is substantial overlap between the prompt quenchers and both the early and late quenchers in their subhalo mass distributions. The subhalo masses of prompt quenchers encompass almost the entire range of subhalo masses for both early and late quenchers. These trends indicate that while mass plays an important role in mediating the time of quenching, it is not the only factor driving quenching in these systems.

5.3 Backsplash systems

The previous section demonstrated that surviving satellites within R_{200} can have complex interactions with their hosts over many Gyrs. In this section, we expand our analysis to satellites beyond R_{200} (out to 1 Mpc) and explore other metrics for quantifying 'infall time.'

There are several categories of systems in the volume that extends out to 1 Mpc: systems that have never entered the host R_{200} (35 per cent of all systems); systems that enter the host R_{200} at high redshift, but exit again, and do not return by redshift zero (24 per cent); systems that enter the host R_{200} exit again, but do return by redshift zero (22 per cent); and systems that enter R_{200} (typically at later times) and remain within R_{200} until redshift zero (19 per cent). Another way of quantifying the exchange of systems across the host's R_{200} that occurs over the course of the simulation is to say that of the systems beyond R_{200}, but within 1 Mpc at $z = 0$, 41 per cent have at some point crossed within R_{200} prior to $z = 0$, and of the systems within R_{200} at $z = 0$, 53 per cent have spent some amount of time after first infall outside R_{200}.

Fig. 13 compares the distributions of the initial infall time ($t_{\rm infall}^{\rm init}$) and the final infall time ($t_{\rm infall}^{\rm fin}$), which is the time when satellites within R_{200} last crossed R_{200}. This plot shows the bimodal distribution of initial infall times, but now it is apparent that the late-infall peak is composed exclusively of systems that have only crossed within R_{200} one time and remained within R_{200} for the rest of the simulation. For these systems, the initial and final infall times are equal ($t_{\rm infall}^{\rm init} = t_{\rm infall}^{\rm fin}$).

There are some early-infalling systems that also remain within R_{200} for the entire simulation, but most of the early-infall peak is composed of returning 'backsplash galaxies,' i.e. systems that had their first encounter with the host galaxy at high redshift, but have only recently returned to the host. The quantity R_{200} does grow with time as the universe expands and the host haloes increase in mass, but for many hosts, the growth in R_{200} is within a factor of 2 over the past 8 Gyr.

A result of this pattern is that the deficit of systems with initial infall times around 4 Gyr ago can be accounted for by expanding this analysis to systems beyond R_{200}. Among systems beyond R_{200} (but within 1 Mpc) that have had an interaction with the host halo, the most common initial infall time lies within the gap found among systems within R_{200}. This is shown in Fig. 13. The distribution of initial infall times among all systems within 1 Mpc does not exhibit the same degree of bimodality.

Fig. 14 shows that backsplash systems beyond R_{200} demonstrate quenching differences as compared to systems of the same stellar mass that have never interacted with the host. The difference between systems in these two groups is most pronounced at a stellar mass of 10^7 M$_\odot$, where only 20 per cent of systems that have never interacted with the host are quenched versus a quenched fraction of 70 per cent for backsplash systems. Indeed, backsplash systems

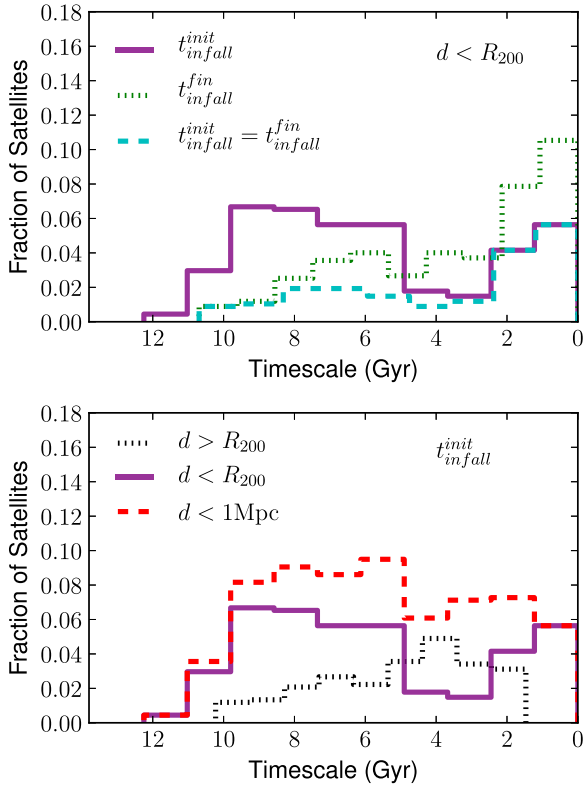

Figure 13. Top: Distributions of infall lookback times for satellites that end the simulation within R_{200}. Two different definitions of infall time are explored: $t^{\rm init}_{\rm infall}$, the time when the satellite first crosses R_{200}, and $t^{\rm fin}_{\rm infall}$, the final time the satellite crosses within R_{200}. Distributions of these time-scales are shown, along with the distribution of satellites for which $t^{\rm init}_{\rm infall}$ and $t^{\rm fin}_{\rm infall}$ are equal. These systems cross within R_{200} once and remain within R_{200} until the end of the simulation. The fraction of satellites plotted is the number of satellites in each bin divided by the total number of satellites within 1 Mpc (673). Bottom: Distributions of $t^{\rm init}_{\rm infall}$ for systems in different distance samples. Systems beyond R_{200} that are included in this plot are backsplash satellites: systems that have been within R_{200} of the main host sometime during their history, but are beyond R_{200} at $z = 0$.

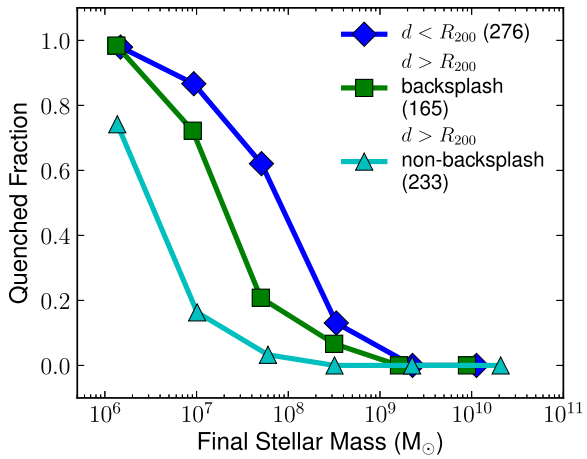

Figure 14. The fraction of quenched subhaloes versus final stellar mass at redshift zero. The trend is shown for three different samples of systems: subhaloes within R_{200} at redshift zero (blue diamonds), subhaloes beyond R_{200} at redshift zero, but which have been within the host R_{200} at some time in the past (green squares), and subhaloes beyond R_{200} that have never been within R_{200} (cyan triangles). The number of systems in each sample is indicated.

beyond R_{200} share a quenching distribution that is very similar to systems within R_{200}.

6 DISCUSSION

6.1 Quenching in the Local Group and its environs

How does star formation in the simulated satellite systems presented here compare to the satellite systems of the Local Group? It should first be noted that the Auriga simulations model haloes similar to the MW in terms of mass and central galaxy properties, but the overall environment of the Auriga haloes (within 1 Mpc) is quite different from the real MW, which has the close neighbour M31 $\sim$ 700 kpc away. There are likely circumgroup environment effects in addition to the circumgalactic environment.

Despite this difference, some aspects of Local Group satellite systems are reproduced. Within 300 kpc of the MW, only two (the LMC and SMC) satellite galaxies are unquenched, out of a total of 10 known systems above our stellar mass cut. This yields an overall quenched fraction of 80 per cent. All systems with a stellar mass at or above 4.6×10^7 M$_\odot$ (the stellar mass of the SMC) are unquenched, also consistent with the Auriga satellites (see Fig. 5). Within M31, there is a similar picture: within 300 kpc, the overall quenched fraction is greater than 80 per cent. These quenched fractions are broadly consistent with the degree of quenching found in the Auriga sample; within 300 kpc, 13 of the Auriga host haloes have quenched fractions above 80 per cent and 17 have quenched fractions below 80 per cent. There may be undiscovered satellites within the MW and M31. These systems are more likely to be quenched, given the low surface brightness of dSphs, and would increase the overall quenched fraction for each host. The Auriga satellite systems are quite different from the satellite systems of the SAGA survey (Geha et al. 2017) that finds uniformly star-forming satellite systems in 8 MW analogue galaxies down to a satellite luminosity of $M_r = -12.3$.

Our simulations produce a very steep quenching trend with stellar mass with a quenched fraction of $\sim$30 per cent at $M_{\rm star} = 10^8$ M$_\odot$ and a quenched fraction $\sim$90 per cent at $M_{\rm star} = 10^6$ M$_\odot$. Observational studies of satellite galaxies at these luminosities do not present a consistent picture of this trend; however, most find a less steep trend than simulated here. Weisz et al. (2015) find a much shallower slope within the Local Group from an analysis of resolved stellar populations, with an especially high-quenched fraction at $M_{\rm star} = 10^8$ M$_\odot$ of over 50 per cent. Slater & Bell (2014) also find a shallower quenching trend with mass with Local Group data from the NASA-Sloan Atlas, but do find the shift in quenched fraction to occur at a stellar mass of 10^7 M$_\odot$, consistent with our results. The data of Karachentsev, Makarov & Kaisina (2013) of galaxies within the local volume ($\leq$11 Mpc) give a much steeper slope for satellite galaxies based on galaxy types, with a lower quenched fraction at 10^8 M$_\odot$, but the quenched fraction at 10^6 M$_\odot$ is less than 70 per cent, lower than the 90 per cent quenched fraction in Auriga (Weisz et al. 2015). It should be noted that both samples lack completeness and apply to environments not directly analogous to the environment simulated here, especially in the case of Karachentsev et al. (2013), whose sample includes satellites around a more heterogeneous group of hosts.

Our simulations also produce a quenching trend with distance (Fig. 5) and the Local Group does demonstrate a correlation between environment and galaxy type, with dSphs being more clustered around the MW and M31 and dIrrs being more common at larger distances (with the exception of the Magellanic Clouds). Geha et al.

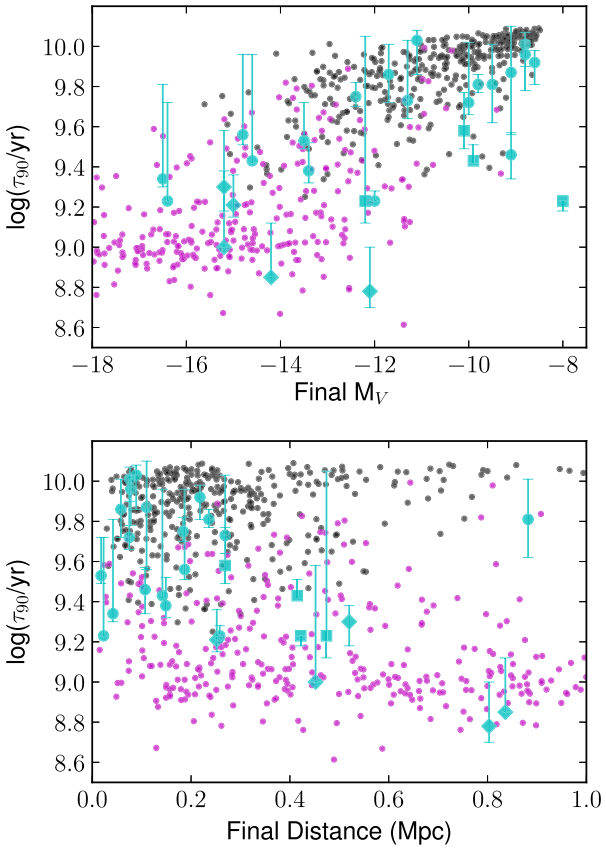

Figure 15. Time-scale τ_{90} plotted versus V-band absolute magnitude (top panel) and final distance from host (bottom panel). τ_{90} is the lookback time when a system has formed 90 per cent of its stellar mass. All satellites in our sample (systems that have a final halo mass above $10^8\,M_\odot$, a final stellar mass above $5 \times 10^5\,M_\odot$, and a final distance less than 1 Mpc) are plotted. Quenched systems are plotted in black and star-forming systems are plotted in magenta. Observational measurements of τ_{90} for Local Group systems from Weisz et al. (2015) are plotted in cyan. We include systems with $M_V \leq -8$ and a distance to the nearest large galaxy (either the MW or M31) less than 1 Mpc. Early-type systems (dSphs and dwarf ellipticals) are plotted with circles; dwarf irregulars are plotted with diamonds; and transitional dwarfs (systems with evidence of recent star formation in their colour–magnitude diagrams, but no Hα emission) are plotted with squares.

(2012) found that quenched field galaxies between $10^7\,M_\odot$ and $10^9\,M_\odot$ are extremely rare, consistent with our findings; however, our most isolated systems are not as isolated as their field sample.

In terms of quenching times, our sample is consistent with observational measurements of τ_{90} from resolved stellar population studies (Weisz et al. 2015). Fig. 15 shows this comparison and, like observed systems, there is a dearth of high-luminosity, early-τ_{90} systems and low-luminosity, late-τ_{90} systems. There are a few notable inconsistencies. While observed dSphs and dEs tend to lie with simulated quenched systems and observed dTrans and dIrr systems tend to lie with simulated unquenched systems, the two prominent dEs of M31, M32 and NGC 205, have values of τ_{90} later than most quenched systems in our sample and that are more consistent with our unquenched systems. Also, while low-luminosity-quenched systems in our sample have values of τ_{90} consistent with dSphs of similar luminosity, they tend to quench somewhat earlier than the typical observed system. In addition, although our sample does not extend down to the luminosity of Leo T, Leo T has an unusually late τ_{90} value for its luminosity with respect to both other observed systems and the trend of our simulated sample.

These results combined with our characterization of satellite infall times confirm previous modelling of dark-matter-only simulations that found that short quenching time-scales relative to satellite infall times (less than 2 Gyr) are required to reproduce the quenched state of Local Group satellite galaxies (Fillingham et al. 2015; Slater & Bell 2014; Wetzel, Tollerud & Weisz 2015).

We found in Auriga a number of 'backsplash' satellite galaxies and demonstrated that their quenching properties are distinct from field systems of similar mass that have never had an encounter with the central host (Fig. 14). Previous work done with cosmological n-body simulations has also found populations of backsplash dwarf galaxies in a Local Group context and demonstrated that they have distinct orbital dynamics from other field populations (Teyssier, Johnston & Kuhlen 2012) and can explain the properties of smaller galaxies surrounding groups and clusters (Wetzel et al. 2014).

6.2 The physics of ram pressure stripping and quenching

Comparisons to the Local Group suggest that despite our model's success at capturing general trends, subhaloes in our sample are perhaps underquenched at high masses and overquenched at low masses. For low-mass systems, this overquenching appears to happen at early times.

A likely explanation of this trend is the stellar feedback and ISM model employed in the Auriga simulations. The Auriga simulations use the subgrid ISM model of Springel & Hernquist (2003) in which dense molecular gas (and low-temperature cooling) is not directly simulated; rather, molecular gas is assumed to be below the resolution of gas cells and its impact on the galaxy is treated in a 'subgrid' fashion: it is assumed to be in pressure equilibrium of the hot phase of the ISM and this pressure is imposed for gas above the star-formation density threshold. However, by not directly simulating molecular clouds, we are also not directly simulating the effects of ram pressure on the molecular phase of the ISM. Idealized simulations of ram pressure stripping at high resolution that model a multiphase medium find that clumps with the density of molecular clouds are able to survive certain low-ram pressure circumstances and that lower density gas is stripped more easily (Tonnesen & Bryan 2009).

Several studies have explored the impact of star formation and internal feedback on ram pressure stripping and have found that it is a minor effect both on the cluster and MW scales (Tonnesen & Bryan 2012; Emerick et al. 2016). However, the feedback model in Auriga is also responsible for the properties and evolution of the CGM and likely impacts the effectiveness of ram pressure stripping by contributing to the density of the CGM. Future studies will explore the CGM properties of the Auriga simulations.

Auriga's ISM and feedback model also appears to regulate a gas-star formation equilibrium for isolated subhaloes with a constant central gas fraction and a continuous SFR that scales with the halo mass (see Fig. 6). Modelling stellar feedback effects in a realistic ISM may be necessary to capture the stochastic aspects of starbursts that may lead to quenching within higher-mass subhaloes, especially systems that are being 'starved', i.e. systems that have their gas supply cut-off due to their proximity to the larger host and are left to consume their existing gas supply. Studies of the dynamics of Local Group satellites indeed suggest that there is a shift in the quenching mechanism of satellites above $10^8\,M_\odot$ and that starvation, where the quenching time becomes the cold gas depletion time, is consistent with observations (Wheeler et al. 2014;

Fillingham et al. 2015). Auriga's ability to capture this mode of quenching is therefore dependent on the ISM and feedback model, which is not tuned to reproduce satellite quenching itself, but rather the cosmic star formation history and abundance matching constraints for central galaxies and lacks a bursty mode of star formation.

6.3 Satellite quenching in different environments

Previous simulations have explored quenching and gas depletion in satellite galaxies in more massive host haloes, including galaxy clusters and groups. These studies typically do not have the baryon resolution to capture the low-mass satellites that we examine, but are able to examine quenching processes in more massive host haloes and out to larger host distances. Bahé et al. (2013) found environmental quenching around hosts above $10^{13}\,M_\odot$ in mass out to $5R_{200}$. The degree of quenching was dependent on the host mass, satellite mass, and the satellite distance. At their lowest host mass, $10^{13}\,M_\odot$ in total mass, and lowest satellite mass, $10^9\,M_\odot$ in stars, they found quenching began within $3R_{200}$ and reached over 80 per cent within R_{200}. Our simulations found no quenching in satellites of this luminosity, perhaps indicating a sharp break in quenching behaviour in host haloes between 10^{12} and $10^{13}\,M_\odot$. In a follow-up study, Bahé & McCarthy (2015) found quenching of their lowest luminosity satellites ($<10^{10}\,M_\odot$ in stars) is very rapid. We also find rapid quenching for many systems, but it does not appear to be strictly a function of mass in our simulations.

At the scale of the MW, idealized simulations with a constant background CGM density have suggested that ram pressure alone may not be an effective quenching mechanism (Emerick et al. 2016); however, we note that the CGM density in our models changes by more than an order of magnitude between ∼10 and ∼100 kpc, and is clumpy and non-axis symmetric. Fillingham et al. (2016) found that ram pressure in a clumpy CGM can be an effective quenching mechanism at the MW scale capable of quenching ∼90 per cent of infalling satellites based on the properties of local field dwarfs. Future simulations with higher resolution in the CGM will allow us to test the effect of CGM clumpiness in greater detail.

7 CONCLUSIONS

In this paper, we have presented a picture of field dwarf and satellite galaxy quenching as modelled in the Auriga cosmological zoom-in simulations of MW type galaxies in $\sim10^{12}\,M_\odot$ haloes. These simulations reproduce general properties of the satellite systems of the MW and M31 in terms of number and quenched fraction. We find that ram pressure stripping is a dominant quenching mechanism and that approximately 50 per cent of satellite systems (systems within R_{200}) quench within 1 Gyr of first infall with their host.

A summary of several key findings:

(i) The Auriga simulations have an average of 11.9 satellites with stellar masses above 5×10^5 within 300 kpc. Subhaloes with this luminosity or greater exhibit a strong mass-dependent quenching pattern, with 90 per cent of systems at $M_{\rm star} \sim 10^6\,M_\odot$ being quenched regardless of distance.

(ii) Systems with $M_{\rm star} < 10^8\,M_\odot$ demonstrate distance-dependent quenching. The distance where increased quenching takes place shifts to smaller distances for lower masses. For the most isolated systems in our sample (beyond 600 kpc), a sharp rise in the quenched fraction occurs below $M_{\rm star} \sim 10^7\,M_\odot$.

(iii) Ram pressure stripping is a ubiquitous phenomenon in lower-mass systems ($M_{\rm star} < 10^7\,M_\odot$) and can produce total gas loss in these systems.

(iv) Other quenching mechanisms we consider are cosmic reionization, stellar feedback, environmental effects, and tidal stripping. We find that by selecting systems with a minimum stellar mass of $5 \times 10^5\,M_\odot$, our sample does not include reionization fossils. Stellar feedback in our model regulates the gas content within dwarf haloes, maintaining a central gas fraction of ∼10 per cent, but lacks the bursty nature to be a dominant quenching mechanism. Larger-scale environmental effects (e.g. interactions with the cosmic web) appear to play an important role for some systems. Tidal effects dramatically impact the dark matter content of satellite systems, but due to the concentration of stellar populations, tidal destruction of the stellar component occurs much later than the disruption of the dark matter.

(v) Of systems within R_{200} at $z = 0$, 51 per cent of quenched systems (37 per cent of all systems) quench within 1 Gyr of first crossing their hosts' R_{200} radius. Systems that quench more than 1 Gyr after first infall tend to be more luminous and systems that quench more than 1 Gyr before first infall tend to be less luminous.

(vi) Systems within R_{200} at $z = 0$ exhibit a bimodality in their infall times, indicative of a dual population within R_{200} of newly in-falling systems and returning backsplash systems that have had a previous interaction with the host. 53 per cent of systems within R_{200} have spent some amount of time outside of R_{200} after their first infall.

(vii) There is a significant population of backsplash systems that fell in earlier and are currently beyond R_{200}. The backsplash population shows quenching properties much like systems with R_{200}. 41 per cent of systems beyond R_{200} but within 1 Mpc at $z = 0$ are backsplash systems.

(viii) The simulated satellites and dwarf galaxies discussed here compare favourably to the systems of the Local Group. One discrepancy is that our estimates for H I gas mass are a factor of a few too high, but the quenching times of our simulated systems broadly agree with observed star formation histories.

This study focused on surviving dwarf galaxies in the vicinity of a MW-type galaxy. These systems are only a portion of the dwarf galaxies that have interacted with the host galaxies over time, and a study of the tidally disrupted systems that do not survive will address important questions such as how the satellites that built the stellar halo at high redshift compare to present-day systems or how did dwarf galaxies contribute to reionization of the local volume.

This study also only touched on dwarf systems with sufficiently resolved stellar components in order to quantify quenching timescales. However, a majority of systems are dark and underluminous, as shown in Fig. 2. Quantifying this population will provide insights into mechanisms for galaxy suppression, not just quenching, and likely include reionization and perhaps environmental effects.

Observational work in this area is in an exciting time. Our ability to probe H I in more diverse environments with the EVLA and SKA pathfinders will yield a more complete picture of gas in different environments beyond the local universe (Fernández et al. 2016). Just recently a ram-pressure stripping candidate around a local MW analogue was discovered with the Westerbork Synthesis Radio Telescope (Hsyu et al. 2017).

This study has demonstrated the power that a large sample of cosmological models with full hydrodynamics can provide in quantifying trends in subhalo properties. Each Auriga halo has a unique history, and while the Auriga haloes all have very similar halo

masses, they can and do have quite a diversity in their substructure properties. In order to understand the underlying physical mechanisms driving evolution in satellite systems as a whole, it is necessary to study them with sufficient statistical power.

ACKNOWLEDGEMENTS

The authors would like to thank the anonymous referee whose comments helped improve this paper. This work has been supported by the European Research Council under ERC-StG grant EXAGAL-308037 and by the Klaus Tschira Foundation. C.M.S. would like to acknowledge helpful conversations with Antonela Monachesi, Greg Bryan, Kathryn Johnston, Mary Putman, Jacqueline van Gorkom, and Stephanie Tonnesen and comments from Adrian Jenkins. R.G. and V.S. acknowledge support by the DFG Research Centre SFB-881 'The Milky Way System' through project A1. Part of the simulations of this paper used the SuperMUC system at the Leibniz Computing Centre, Garching, under the project PR85JE of the Gauss Centre for Supercomputing. This work was supported by the Science and Technology Facilities Council (grant numbers ST/F001166/1 and ST/I00162X/1) and European Research Council (grant number GA 267291 'Cosmiway'). It used the DiRAC Data Centric system at Durham University, operated by the Institute for Computational Cosmology on behalf of the STFC DiRAC HPC Facility (www.dirac.ac.uk). This equipment was funded by BIS National E-infrastructure capital grant ST/K00042X/1, STFC capital grant ST/H008519/1, and STFC DiRAC Operations grant ST/K003267/1 and Durham University. DiRAC is part of the National E-Infrastructure.

REFERENCES

Bahé Y. M., McCarthy I. G., 2015, MNRAS, 447, 969
Bahé Y. M., McCarthy I. G., Balogh M. L., Font A. S., 2013, MNRAS, 430, 3017
Behroozi P. S., Wechsler R. H., Conroy C., 2013, ApJ, 770, 57
Benítez-Llambay A., Navarro J. F., Abadi M. G., Gottlöber S., Yepes G., Hoffman Y., Steinmetz M., 2013, ApJ, 763, L41
Benson A. J., Lacey C. G., Baugh C. M., Cole S., Frenk C. S., 2002, MNRAS, 333, 156
Blitz L., Rosolowsky E., 2006, ApJ, 650, 933
Boylan-Kolchin M., Bullock J. S., Kaplinghat M., 2011, MNRAS, 415, L40
Collins M. L. M. et al., 2013, ApJ, 768, 172
Davis M., Efstathiou G., Frenk C. S., White S. D. M., 1985, ApJ, 292, 371
De Lucia G., Blaizot J., 2007, MNRAS, 375, 2
Drlica-Wagner A. et al., 2015, ApJ, 813, 109
Efstathiou G., 1992, MNRAS, 256, 43P
Emerick A., Mac Low M.-M., Grcevich J., Gatto A., 2016, ApJ, 826, 148
Fattahi A. et al., 2016, MNRAS, 457, 844
Faucher-Giguère C.-A., Lidz A., Zaldarriaga M., Hernquist L., 2009, ApJ, 703, 1416
Fernández X. et al., 2016, ApJ, 824, L1
Fillingham S. P., Cooper M. C., Wheeler C., Garrison-Kimmel S., Boylan-Kolchin M., Bullock J. S., 2015, MNRAS, 454, 2039
Fillingham S. P., Cooper M. C., Pace A. B., Boylan-Kolchin M., Bullock J. S., Garrison-Kimmel S., Wheeler C., 2016, MNRAS, 463, 1916
Fitts A. et al., 2017, MNRAS, 471, 3547
Garrison-Kimmel S., Boylan-Kolchin M., Bullock J. S., Lee K., 2014, MNRAS, 438, 2578
Gatto A., Fraternali F., Read J. I., Marinacci F., Lux H., Walch S., 2013, MNRAS, 433, 2749
Geha M., Blanton M. R., Yan R., Tinker J. L., 2012, ApJ, 757, 85
Geha M. et al., 2017, ApJ, 847, 4
Gnedin N. Y., 2000, ApJ, 542, 535
Grand R. J. J. et al., 2017, MNRAS, 467, 179
Grcevich J., Putman M. E., 2009, ApJ, 696, 385
Grebel E. K., 1999, in Whitelock P., Cannon R., eds, Proc. IAU Symp. 192, The Stellar Content of Local Group Galaxies. Astron. Soc. Pac., San Francisco, p. 17
Gunn J. E., Gott III J. R., 1972, ApJ, 176, 1
Guo Q., White S., Li C., Boylan-Kolchin M., 2010, MNRAS, 404, 1111
Hellwing W. A., Frenk C. S., Cautun M., Bose S., Helly J., Jenkins A., Sawala T., Cytowski M., 2016, MNRAS, 457, 3492
Hoeft M., Yepes G., Gottlöber S., Springel V., 2006, MNRAS, 371, 401
Hsyu T., Cooke R. J., Prochaska J. X., Bolte M., 2017, ApJ, 845, L22
Huxor A. P. et al., 2011, MNRAS, 414, 770
Ibata R. A. et al., 2013, Nature, 493, 62
Jenkins A., 2010, MNRAS, 403, 1859
Karachentsev I. D., Makarov D. I., Kaisina E. I., 2013, AJ, 145, 101
Kirby E. N., Martin C. L., Finlator K., 2011, ApJ, 742, L25
Klypin A., Kravtsov A. V., Valenzuela O., Prada F., 1999, ApJ, 522, 82
Koposov S. E., Belokurov V., Torrealba G., Evans N. W., 2015, ApJ, 805, 130
Leroy A. K., Walter F., Brinks E., Bigiel F., de Blok W. J. G., Madore B., Thornley M. D., 2008, AJ, 136, 2782
Makarova L. N., Makarov D. I., Karachentsev I. D., Tully R. B., Rizzi L., 2017, MNRAS, 464, 2281
Marinacci F., Pakmor R., Springel V., 2014, MNRAS, 437, 1750
Marinacci F., Grand R. J. J., Pakmor R., Springel V., Gómez F. A., Frenk C. S., White S. D. M., 2017, MNRAS, 466, 3859
McConnachie A. W., 2012, AJ, 144, 4
McGaugh S. S., Schombert J. M., de Blok W. J. G., Zagursky M. J., 2010, ApJ, 708, L14
Moore B., Ghigna S., Governato F., Lake G., Quinn T., Stadel J., Tozzi P., 1999, ApJ, 524, L19
Okamoto T., Frenk C. S., 2009, MNRAS, 399, L174
Okamoto T., Gao L., Theuns T., 2008, MNRAS, 390, 920
Okamoto T., Frenk C. S., Jenkins A., Theuns T., 2010, MNRAS, 406, 208
Pakmor R., Bauer A., Springel V., 2011, MNRAS, 418, 1392
Pakmor R., Springel V., Bauer A., Mocz P., Munoz D. J., Ohlmann S. T., Schaal K., Zhu C., 2016, MNRAS, 455, 1134
Planck Collaboration XVI, 2014, A&A, 571, A16
Powell K. G., Roe P. L., Linde T. J., Gombosi T. I., De Zeeuw D. L., 1999, J. Comput. Phys., 154, 284
Roediger E., Hensler G., 2005, A&A, 433, 875
Ryan-Weber E. V., Begum A., Oosterloo T., Pal S., Irwin M. J., Belokurov V., Evans N. W., Zucker D. B., 2008, MNRAS, 384, 535
Safarzadeh M., Scannapieco E., 2017, ApJ, 850, 99
Sawala T., Scannapieco C., Maio U., White S., 2010, MNRAS, 402, 1599
Sawala T. et al., 2016a, MNRAS, 456, 85
Sawala T. et al., 2016b, MNRAS, 457, 1931
Schaye J. et al., 2015, MNRAS, 446, 521
Shen S., Madau P., Conroy C., Governato F., Mayer L., 2014, ApJ, 792, 99
Simpson C. M., Bryan G. L., Johnston K. V., Smith B. D., Mac Low M.-M., Sharma S., Tumlinson J., 2013, MNRAS, 432, 1989
Slater C. T., Bell E. F., 2014, ApJ, 792, 141
Springel V., 2010, MNRAS, 401, 791
Springel V., Hernquist L., 2003, MNRAS, 339, 289
Springel V., White S. D. M., Tormen G., Kauffmann G., 2001, MNRAS, 328, 726
Springel V., Di Matteo T., Hernquist L., 2005a, MNRAS, 361, 776
Springel V. et al., 2005b, Nature, 435, 629
Strigari L. E., Bullock J. S., Kaplinghat M., Simon J. D., Geha M., Willman B., Walker M. G., 2008, Nature, 454, 1096
Teyssier M., Johnston K. V., Kuhlen M., 2012, MNRAS, 426, 1808
Thoul A. A., Weinberg D. H., 1996, ApJ, 465, 608
Tonnesen S., Bryan G. L., 2009, ApJ, 694, 789
Tonnesen S., Bryan G. L., 2012, MNRAS, 422, 1609
Vogelsberger M., Genel S., Sijacki D., Torrey P., Springel V., Hernquist L., 2013, MNRAS, 436, 3031
Weisz D. R., Dolphin A. E., Skillman E. D., Holtzman J., Gilbert K. M., Dalcanton J. J., Williams B. F., 2014, ApJ, 789, 147

Weisz D. R., Dolphin A. E., Skillman E. D., Holtzman J., Gilbert K. M., Dalcanton J. J., Williams B. F., 2015, ApJ, 804, 136
Wetzel A. R., Tinker J. L., Conroy C., van den Bosch F. C., 2014, MNRAS, 439, 2687
Wetzel A. R., Tollerud E. J., Weisz D. R., 2015, ApJ, 808, L27
Wetzel A. R., Hopkins P. F., Kim J.-h., Faucher-Giguère C.-A., Kereš D., Quataert E., 2016, ApJ, 827, L23
Wheeler C., Phillips J. I., Cooper M. C., Boylan-Kolchin M., Bullock J. S., 2014, MNRAS, 442, 1396
Zhu Q., Marinacci F., Maji M., Li Y., Springel V., Hernquist L., 2016, MNRAS, 458, 1559
Zolotov A. et al., 2012, ApJ, 761, 71

APPENDIX: RESOLUTION AND CONVERGENCE

In this appendix, we explore the impact of numerical resolution on the satellite system properties. We do this by comparing the 30 Auriga zoom simulations discussed in the main text to six resimulations of Auriga haloes with a factor of 8 better mass resolution as described in Grand et al. (2017). We especially focus on lower mass satellite systems since they have fewer resolution elements.

Table A1 lists the satellite properties of the six zoom simulations from our halo suite that have a target cell mass of 6×10^3 M$_\odot$ and minimum softening length of 184 pc at $z = 0$ for high resolution dark matter particles and star particles. We call these simulations 'Level 3' resolution simulations and the standard resolution simulations listed in Table 1 'Level 4' resolution simulations.

The stellar mass threshold we adopt in the main text is 10 times the typical mass of a star particle at Level 4 resolution. With eight times better mass resolution, systems at this stellar mass limit in the Level 3 runs should have approximately 80 star particles.

Fig. A1 shows how the luminosity distributions compare between haloes simulated with the same initial conditions, but with different mass resolution. There are small differences in the stellar masses of some satellites, but the overall luminosity distributions follow each other between resolution levels. The final numbers of satellites are similar down to the stellar mass threshold we adopt, with only a slight excess of satellites in the Level 3 simulations.

Fig. A2 compares the quenched fractions of dwarf galaxies between the Level 3 and Level 4 resolution simulations. The characteristic up-turn in the fraction of quenched systems with stellar masses below 10^7 M$_\odot$ is apparent in the Level 3 simulations to a

Table A1. Subhalo population properties by host halo for the high-resolution Level 3 simulations.

Simulation	Host M_{200} (10^{12} M$_\odot$)	Host R_{200} (kpc)	$N_{\rm sub}$ (<300 kpc/1 Mpc)	max($v v_{\rm max}$) (km s^{-1})	$f_{\rm quenched}$ (<300 kpc/1 Mpc)	$f_{\rm HIpoor}$ (<300 kpc/1 Mpc)	min($M_{\rm H\,I} > 0$) (10^6 M$_\odot$)
Au6	1.01	212	8/13	93	0.5/0.38	0.5/0.31	2.14
Au16	1.5	242	15/29	117	0.67/0.48	0.67/0.45	0.74
Au21	1.42	237	17/35	108	0.65/0.46	0.65/0.43	0.82
Au23	1.5	242	16/22	51	0.75/0.64	0.81/0.64	8.13
Au24	1.47	240	14/37	120	0.64/0.41	0.57/0.32	0.85
Au27	1.7	251	13/18	113	0.69/0.61	0.69/0.61	1.55

Note. The quantities presented in each column are the same as Table 1 except for the final column, which is the lowest positive H I mass found in satellites of the host.

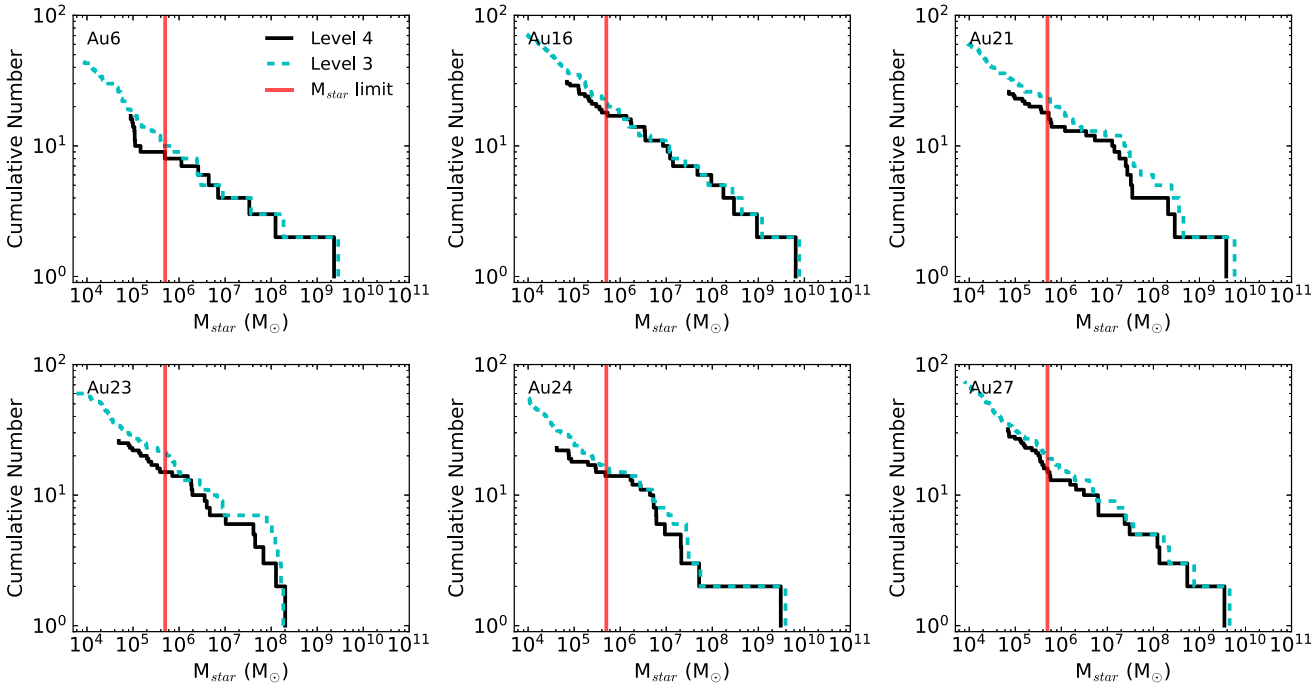

Figure A1. Cumulative distributions of the final satellite stellar masses for Auriga host haloes simulated at both the high Level 3 mass resolution (dashed cyan) and the low Level 4 mass resolution (solid black). The mass resolution in the two sets of simulations differ by a factor of 8. The stellar mass limit (5×10^5 M$_\odot$) adopted for the analysis in the main text of the paper is shown with a vertical red line.

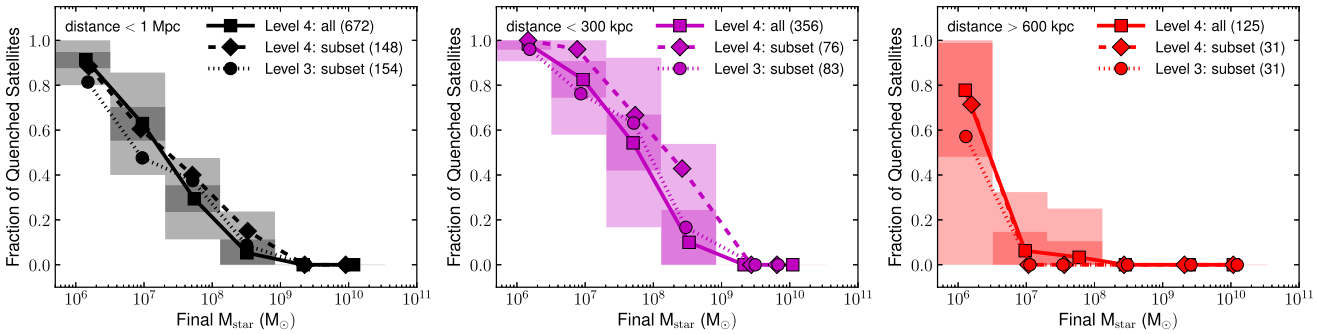

Figure A2. Comparison of the quenched fractions of dwarf systems as a function of final stellar mass between the Level 4 simulations and the higher-resolution Level 3 simulations. We separate dwarf systems into three distance bins in the three panels shown: all systems within 1 Mpc (black, left-hand panel), systems within 300 kpc (magenta, centre panel), and systems beyond 600 kpc, but within 1 Mpc (red, right-hand panel). The quenched fraction of systems in all 30 Level 4 haloes (solid lines with squares) are shown in the same way as in Fig. 5 in each distance bin. Trends for all systems in the six Level 3 haloes are shown (dotted lines with circles) and trends for all systems in the six Level 4 haloes that match the Level 3 haloes (dashed lines with squares). Shaded regions show the range of quenched fractions produced by 10^4 randomly selected sets of six distinct Level 4 haloes. The light-shaded regions show the 3σ range in the quenched fraction around the mean and the dark shaded regions show the 1σ range. Higher-mass bins do not show a range of values because, above a certain stellar mass, all systems are star forming (as described in Section 3.3).

similar degree as the Level 4 simulations. It should be noted however, that at large distances especially, the smaller number of dwarf systems in the Level 3 simulations introduces a larger scatter in fractional results. From this analysis, we conclude that the evolution of low-mass systems is numerically converged with our model.

Table A1 lists the lowest non-zero H I masses found in satellites of each host halo within 1 Mpc. These values are computed with the same methods and limits as the results in the main section of the text. These values are similar to the lowest values found in the Level 4 simulations. The additional of resolution of the Level 3 runs does not allow us to capture satellites with lower H I masses, mainly because this calculation relies on assumptions of our subgrid model and is therefore insensitive to resolution.

This paper has been typeset from a TEX/LATEX file prepared by the author.